



**BAND GAP TRANSITION STUDIES OF U:THO<sub>2</sub> USING  
CATHODOLUMINESCENCE**

THESIS

Joshua D. Reding, Second Lieutenant, USAF

AFIT-ENP-14-M-31

**DEPARTMENT OF THE AIR FORCE  
AIR UNIVERSITY**

***AIR FORCE INSTITUTE OF TECHNOLOGY***

**Wright-Patterson Air Force Base, Ohio**

DISTRIBUTION STATEMENT A:  
APPROVED FOR PUBLIC RELEASE; DISTRIBUTION UNLIMITED

The views expressed in this thesis are those of the author and do not reflect the official policy or position of the United States Air Force, the Department of Defense, or the United States government.

This material is declared a work of the U.S. government and is not subject to copyright protection in the United States.

AFIT-ENP-14-M-31

BAND GAP TRANSITION STUDIES OF U:THO<sub>2</sub> USING  
CATHODOLUMINESCENCE

THESIS

Presented to the Faculty  
Department of Engineering Physics  
Graduate School of Engineering and Management  
Air Force Institute of Technology  
Air University  
Air Education and Training Command  
in Partial Fulfillment of the Requirements for the  
Degree of Master of Science in Applied Physics

Joshua D. Reding, B.S.  
Second Lieutenant, USAF

March 2014

DISTRIBUTION STATEMENT A:  
APPROVED FOR PUBLIC RELEASE; DISTRIBUTION UNLIMITED

BAND GAP TRANSITION STUDIES OF U:THO<sub>2</sub> USING  
CATHODOLUMINESCENCE

Joshua D. Reding, B.S.  
Second Lieutenant, USAF

Approved:

\_\_\_\_\_  
//signed//  
Robert L. Hengehold, PhD (Chair)

\_\_\_\_\_  
12 March 2014  
Date

\_\_\_\_\_  
//signed//  
Lt Col Stephen R. McHale, PhD (Member)

\_\_\_\_\_  
12 March 2014  
Date

\_\_\_\_\_  
//signed//  
David B. Turner, PhD (Member)

\_\_\_\_\_  
12 March 2014  
Date



**Abstract**

The Department of Defense has expressed interest in thorium dioxide ( $\text{ThO}_2$ ) and uranium dioxide ( $\text{UO}_2$ ) as possible candidates for use as special nuclear material in designing neutron detectors. Both materials have large neutron interaction cross sections. Uranium dioxide is particularly attractive due to its semiconducting properties and a relatively small band gap of 2 eV. Both materials fluoresce under ionizing radiation making them candidates for scintillating detectors.

Three  $\text{U}_x\text{:Th}_{1-x}\text{O}_2$  ( $x = 0.00, 0.01, 0.22$ ) hydrothermally grown single crystals were examined using cathodoluminescence to interrogate the changing electronic properties of  $\text{ThO}_2$  as it became an alloy. Both depth-resolved and temperature-dependent cathodoluminescence studies were performed to examine the crystal structure and the defects present. An ultra-high vacuum system operating at  $10^{-8}$  Torr was used with electron beam energies ranging from 2 to 14 keV. Spectra were taken on all three samples before and after a proprietary chemical cleaning process involving a crown ether/picric acid solution was applied to the crystals to remove surface contaminants.

Spectral deconvolution of the spectra showed evidence of both direct and indirect gap photon transitions from the O 2p to Th 6d at 4.2 eV and 4.8 eV respectively. Uranium-doped spectra showed evidence of the midgap O 2p to U 5f quadrupole transition and O 2p to U 6d transition at 5 eV.

*To my Lord Jesus Christ, through whom all things are possible*

## **Acknowledgments**

First and foremost, I would like to thank my Lord and Savior Jesus Christ for granting me the resolve and intellect to finish this document even when I did not necessarily believe it to be possible myself. Without his aid, this document would not have been completed. Next, Dr. Robert Hengehold, my advisor, and Dr. David Turner, my mentor, were invaluable at every step of the process, not only in dispensing guidance and wisdom, but in allowing me to make my own mistakes and struggle to solve problems and blaze my own trail. I would like to thank the third member of my committee, LTC Stephen McHale for his time and efforts in assisting me with this project. I would not have nearly the complete thesis that I do without the efforts of Dr. Tony Kelly, who was instrumental in aiding me in reaching my conclusions. I would like to thank the technicians Greg Smith and Mike Ranft for their expertise in operating the systems and their boundless patience. Also, Major Michael Lee, who built the system I performed my research on, and who pulled me into this project in the beginning.

I would not be here without my professors, Corey Gavitt and Jerney Cipiti who first encouraged me to a career in science in addition to the AFROTC Detachment 510 cadre, LTC (retired) Raul Garcia, Major Christopher Fitzgerald, Major Scott McMahon, Major Jennifer Bradley, TSgt Julie Carr, and SSgt Theresa Williams who made my entry into AFIT and the Air Force possible. My gratitude goes out to all my family and friends both here in Ohio and elsewhere who put up with me through the last eighteen months of anxiety and stress. Finally, I would like to thank the Air Force Institute of Technology and the Air Force for giving me this incredible opportunity to be a better officer. I could not have accomplished this without any of the above mentioned people, as well as many others.

Joshua D. Reding

## Table of Contents

	Page
Abstract . . . . .	iv
Dedication . . . . .	v
Acknowledgments . . . . .	vi
Table of Contents . . . . .	vii
List of Figures . . . . .	x
List of Tables . . . . .	xii
List of Symbols . . . . .	xiii
List of Acronyms . . . . .	xv
 I. Introduction . . . . .	 1
1.1 Motivation . . . . .	1
1.2 Research Topic . . . . .	3
1.3 Research Objective . . . . .	4
1.4 Crystals . . . . .	5
 II. Theoretical Background . . . . .	 9
2.1 Atomic Properties of $U_x:Th_{1-x}O_2$ . . . . .	9
2.2 Electronic Structure of $U_x:Th_{1-x}O_2$ . . . . .	11
2.3 Previous Studies . . . . .	14
2.4 Luminescence Processes in Solids . . . . .	17
2.5 Depth-Resolved Cathodoluminescence . . . . .	21
2.6 Temperature-Dependent Cathodoluminescence . . . . .	26
2.7 X-ray Fluorescence . . . . .	27
 III. Methodology . . . . .	 28
3.1 Experimental Approach . . . . .	28
3.2 Crystal Fabrication . . . . .	29
3.3 XRF System . . . . .	30

	Page
3.4 CASINO . . . . .	31
3.5 Cathodoluminescence System Design . . . . .	32
3.5.1 Main Chamber . . . . .	32
3.5.2 Vacuum Methods . . . . .	33
3.5.3 Cryo Cooler . . . . .	35
3.5.4 Electron Gun . . . . .	36
3.6 Optics and Monochromator . . . . .	38
3.7 Signal-To-Noise Ratio Improvement Techniques . . . . .	40
3.8 Sources of Error . . . . .	41
3.8.1 Filament Spectrum . . . . .	41
3.8.2 Temperature . . . . .	42
3.9 Cleaning Process . . . . .	42
3.10 Software . . . . .	45
IV. Results and Analysis . . . . .	46
4.1 XRF . . . . .	46
4.1.1 XRF Results for 003 TU . . . . .	48
4.1.2 XRF Results for 041 TU . . . . .	51
4.2 CASINO Simulations . . . . .	52
4.3 Undoped ThO <sub>2</sub> Post-Cleaning . . . . .	54
4.4 Cathodoluminescence of Lightly-Doped U:ThO <sub>2</sub> . . . . .	59
4.4.1 Pre-Cleaning . . . . .	59
4.4.2 Post-Cleaning . . . . .	62
4.5 Cathodoluminescence Heavily-Doped U:ThO <sub>2</sub> . . . . .	67
4.5.1 Pre-Cleaning . . . . .	67
4.5.2 Post-Cleaning . . . . .	69
V. Conclusion . . . . .	73
5.1 Summary of Results . . . . .	73
5.1.1 XRF and Chemical Cleaning . . . . .	73
5.1.2 Cathodoluminescence . . . . .	73
5.2 Future Research . . . . .	75
Appendix A: CL System Parts List . . . . .	77
Appendix B: Deconvolution Table . . . . .	78
Appendix C: CL Spectral Data . . . . .	79

	Page
Appendix D: Supplementary Casino Data . . . . .	81
References . . . . .	85

## List of Figures

Figure	Page
1.1 Undoped ThO <sub>2</sub> crystal, 001 TO after cleaning . . . . .	6
1.2 Lightly-doped U:ThO <sub>2</sub> crystal, 003 TU before cleaning . . . . .	6
1.3 Lightly-doped U:ThO <sub>2</sub> crystal, 003 TU after cleaning . . . . .	7
1.4 Heavily-doped thorium oxide crystal 041 TU before cleaning . . . . .	7
1.5 Heavily-doped thorium oxide crystal, 041 TU after cleaning . . . . .	8
2.1 Fluorite crystalline structure of thorium oxide . . . . .	10
2.2 Schematic of electronic transitions . . . . .	20
2.3 7 keV CASINO simulation for electron pathways through 041 TU . . . . .	25
3.1 Horiba XGT-7000 XRF imaging microscope . . . . .	30
3.2 Full view of cathodoluminescence system. . . . .	32
3.3 Schematic of cathodoluminescence system. . . . .	34
3.4 Schematic of electron gun . . . . .	36
3.5 Kimball Electronics electron gun used in the cathodoluminescence system . . .	38
3.6 Schematic diagram of photon pathways through monochromator. . . . .	39
3.7 Crown ether-picric acid solution with 003 TU crystal inside the vial. . . . .	43
4.1 4x5 point XRF grid . . . . .	47
4.2 Elemental analysis spectrum from point ten of a twenty point XRF grid . . . .	48
4.3 3 keV CASINO simulation through 003 TU . . . . .	53
4.4 001 TO post-cleaning DRCL measurements . . . . .	55
4.5 001 TO post-cleaning normalized DRCL measurements . . . . .	56
4.6 001 TO post-cleaning TDCL measurements . . . . .	58
4.7 003 TU pre-cleaning DRCL measurements . . . . .	59
4.8 003 TU pre-cleaning TDCL measurements . . . . .	61

Figure	Page
4.9 003 TU post-cleaning DRCL measurements . . . . .	63
4.10 003 TU post-cleaning TDCL measurements . . . . .	65
4.11 003 TU hysteresis measurements . . . . .	66
4.12 041 TU pre-cleaning DRCL measurements . . . . .	68
4.13 041 TU post-cleaning DRCL measurements . . . . .	70
4.14 041 TU hysteresis measurements . . . . .	71
C.1 Filament spectrum taken for the initial electron gun. . . . .	79
C.2 Filament spectrum taken for the replacement electron gun. . . . .	80
D.1 3 keV CASINO simulation through 003 TU . . . . .	81
D.2 7 keV CASINO simulation for electron pathways through 001 TO . . . . .	82
D.3 10 keV CASINO simulation through 001 TO . . . . .	83
D.4 10 keV CASINO simulation through 003 TU . . . . .	83
D.5 3 keV CASINO simulation through 041 TU . . . . .	84
D.6 10 keV CASINO simulation through 041 TU . . . . .	84



## List of Tables

Table	Page
2.1 A non-hybridization look at the binding reaction of ionized Th & O [11] . . . .	12
2.2 Electron-Hole Generation Factors in U:ThO <sub>2</sub> and ThO <sub>2</sub> . . . . .	18
3.1 Concentrations of Cleaning Solution Reactants . . . . .	44
4.1 Mass Percentage Concentrations Pre- and Post-Cleaning . . . . .	49
4.2 CASINO Average Penetration Depths . . . . .	52
A.1 Equipment List for CL System . . . . .	77
B.1 Deconvolution Spectral Comparison Results . . . . .	78

## List of Symbols

Symbol	Definition
001 TO	undoped ThO <sub>2</sub>
003 TU	lightly doped U:ThO <sub>2</sub>
041 TU	heavily doped U:ThO <sub>2</sub>
$\alpha$	Gruen atomic number value
$A$	atomic weight
$A_e$	Richardson-Dushman constant
$R^2$	Coefficient of determination
$e$	elementary charge of electron
$eV$	energy (electron volts)
$E_A$	energy (acceptor level)
$E_b$	energy (electron beam)
$E_C$	energy (conduction band)
$E_D$	energy (donor level )
$E_g$	energy (band gap)
$E_i$	energy (ionization)
$E_V$	energy (valence band)
$\epsilon$	permittivity of material
$J$	mean ionization potential in Gruen equation
$J_e$	emission current density
$k_B$	Boltzmann's constant
$k$	Gruen constant
$G$	generation factor
$\gamma$	fraction of energy loss due to back scattered electrons

Symbol	Definition
$M$	material constant related to the ionization energy
$\phi$	Work function of cathode
$\rho$	density
$r$	distance between donor and acceptor level
$T$	temperature in Kelvin
$V$	potential applied to the electron gun cathode
$Z$	atomic number

## List of Acronyms

Acronym      Definition

**AFIT** Air Force Institute of Technology

**CASINO** monte CARlo SIMulation of electroN trajectory in sOlids

**CL** Cathodoluminescence

**DAP** Donor-acceptor pair

**DOS** density of states

**DRCL** depth-resolved cathodoluminescence

**e-h** electron-hole

**EXAFS** extended x-ray absorption fine structure

**FWHM** full-width at half maximum

**IVMO** inner valence molecular orbital

**PMT** photomultiplier tube

**SNM** special nuclear material

**S/N** signal-to-noise

**TDCL** temperature-dependent cathodoluminescence

**TOF-SIMS** time of flight-secondary ion mass spectroscopy

**UHV** ultra-high vacuum

Acronym	Definition
---------	------------

<b>XPS</b>	x-ray photoelectron spectroscopy
------------	----------------------------------

<b>XRF</b>	X-ray fluorescence
------------	--------------------

# BAND GAP TRANSITION STUDIES OF U:THO<sub>2</sub> USING CATHODOLUMINESCENCE

## I. Introduction

### 1.1 Motivation

There is a demand for adaptable, efficient, and transportable neutron detectors. The detectors are necessary for a wide variety of uses such as monitoring nuclear materials in energy source applications and preventing asymmetrical-warfare oriented opponents from deploying nuclear weapons. Modern special nuclear material (SNM) detectors are large, bulky and operated at sites such as ports and border crossings; however, these are inadequate to properly monitor the sheer volume of material and personnel entering the country on a day-to-day basis. Furthermore, these are difficult to use for nuclear forensics. A handheld SNM detector would greatly enhance the security of the nation and the safety of its people.

Modern SNM detection methods fall into two categories: neutron and radiation. SNM can emit beta, gamma and x-ray radiation. The most common detectors attempt to identify these SNM markers which can be easily blocked using shielding methods such as lead. Therefore, these detectors are not efficient for the detection of clandestine materials. Being neutrally charged, neutrons rarely interact with materials and require specialized shielding in order to block their transit. As such, a detector that responds to neutron bombardment is more desirable. Neutron interactions occur in two ways: through scattering off the nucleus, or through the instigation of a nuclear reaction. Nucleus scattering results in a transfer of kinetic energy which subsequently ionizes the molecule. Due to the high energy needed in most materials to cause ionization, only H and He are

light enough for this to be practical. A nuclear reaction results in the emission of various products: protons, alpha particles, gammas, etc...[9]. Each of these products is more easily detected than the neutrons themselves. As an added benefit, these reactions occur at thermal energies (meV).

Actinide oxides are attractive candidates for scintillating detectors due to their high neutron interaction cross sections and their propensity to fluoresce in the presence of ionizing radiation. Thorium dioxide (thoria) is a material whose crystalline structure is well-understood, and various electronic structure characterization studies have been conducted. Further, it can be used as a stepping stone toward the investigation of uranium dioxide crystals. Uranium dioxide (urania) is an attractive candidate for a detector due to its smaller band gap and high neutron interaction cross section, three times that of thorium dioxide [16]. In order to fully understand and characterize uranium dioxide, single crystal thorium dioxide with increasing uranium dopant concentrations were characterized in this research.

Furthermore, the search for non-fossil fuel energy sources is a principal goal for world leaders. The naturally occurring thorium-232 ( $^{232}\text{Th}$ ) is an ideal candidate as a replacement for traditional uranium or plutonium sources in nuclear reactors, due to  $^{232}\text{Th}$  containing smaller amounts of fissile material than the other sources. As a result, thorium is useful for non-proliferation purposes as countries could no longer investigate fissionable uranium under the pretence of energy research. Although the Th fuel cycle needs a lot more study to be made efficient, Th has many attractive qualities as a fuel source beyond just non-proliferation. Thorium is also four times more abundant than uranium in the earth's crust, making it a cheaper alternative to mine [26]. Thorium has a higher melting point than uranium, is more resistant to corrosion, and has a lower thermal expansion coefficient [26, 33]. The thorium fuel cycle also produces low radiotoxicity waste in the form of actinides, such as neptunium, americium, and curium [37]. Atomic and molecular

studies of both uranium-doped and pure thoria and urania are scarce outside the thermal regime and as such have yet to be fully characterized.

This thesis project is a follow-on from the thesis work of Jacob Castilow and Major Michael Lee as well as the dissertation of Tony Kelly [6, 19, 22]. Castilow grew one of the uranium-doped samples used in this thesis research. Major Lee performed depth-resolved cathodoluminescence (DRCL) measurements on the same undoped thorium sample used. T. Kelly performed time of flight-secondary ion mass spectroscopy (TOF-SIMS) measurements on the pure thoria to investigate the surface cleanliness. Lee repeated the DRCL measurements and saw changes in the spectra due to the side effect of TOF-SIMS being localized clean points on the surface. This motivated this thesis which undertook to chemically clean the surface of multiple crystals and examine the difference in the CL spectra pre- and post-cleaning to ascertain information about the outer valence and conduction band structure of the materials.

## 1.2 Research Topic

Characterization of  $U_x:Th_{1-x}O_2$  at progressively higher uranium dopant levels ( $x = 0.00, 0.01, 0.22$ ) is essential in fully characterizing  $UO_2$  in the future and to this end, several investigative tools are used. X-ray fluorescence (XRF) spectroscopy was used to determine the elemental crystal composition and ensure the presence of uranium in the crystal lattice. This process also identifies other elements that exist as surface contaminants or impurities in the single crystal structure. This aids in the interpretation of the luminescence spectrum used to characterize the material. To accomplish this characterization, an ultra-high vacuum system operating at  $10^{-8}$  Torr was used to gather cathodoluminescence spectra of uranium-doped and undoped thoria in the range of 2000-8000Å. A detailed examination of the vacuum system, as well as the set-up for photon collection may be found in Chapter 3. Background research has revealed a wide variety of both thoria and urania. density of states (DOS) models and first-principle



calculations have revealed theoretical band structures that attempt to define the conduction and valence bands and establish a definitive band gap of both pure  $\text{ThO}_2$  and  $\text{UO}_2$ . These calculations proved invaluable in the interpretation of the cathodoluminescence spectrum obtained in this study. Various luminescence and thermal properties studies have been conducted on both thorium and uranium including cathodoluminescence; however, the literature is far from complete. As a nuclear fuel substitute, many of these studies are centered around the thermal expansion and how thorium and uranium react at high temperatures. In regards to luminescence studies, the majority of these are photoluminescence and x-ray photoelectron spectroscopy (XPS) studies, the results of which are discussed in detail in Chapter 2. Further, many of these studies are performed on thin films, powders that under pressure form crystals, or oxidized thorium crystals, not the single crystals that were used in this study. The uniformity found in single crystals minimizes variations in many thermal properties of the material which is beneficial for nuclear energy purposes.

### **1.3 Research Objective**

Uranium doped thorium oxide is a material upon which few studies have been performed. The goal of this research is to determine how the insertion of uranium atoms into the thorium dioxide fluorite crystal lattice changes the electronic structure. It is hypothesized that due to the similarities in the atomic size between the thorium and uranium, emission spectra of uranium-doped thorium dioxide should retain some of the same characteristics of the undoped thorium dioxide such as the  $\text{ThO}_2$  band gap transition. The addition of uranium should cause an increased 5f character to be present in the material which will ideally be seen as an additional peak in the spectrum correlating to the band gap transition of O 2p to U 5f.

Using three hydrothermally grown single crystals with varying levels of uranium dopant, three different studies will be conducted before and after a chemical cleaning

process using a crown-ether/picric acid solution is applied. The cathodoluminescence spectrum changes as the material as the uranium concentration varies (0%, 1%, 23%) and becomes more of an alloy. First, XRF studies will provide information concerning the mass concentration percentages before and after cleaning giving information about the impurities in the material as well as serve as a verification of the uranium concentration of uranium in the material. Next, the monte CARlo SIMulation of electroN trajectory in sOlids (CASINO) program will be used to determine average penetration depths and energy loss of the electrons from the electron gun as they impinge upon the sample surface. This will provide a roadmap for what electron beam energies should be used when conducting experiments. Then, DRCL and temperature-dependent cathodoluminescence (TDCL) experiments will be performed to interrogate the outer valence and conduction band structure of the molecule. This will be accomplished through use of an ultra-high vacuum system operating in a temperature range of 36-316 K. An ultra-high vacuum (UHV) is necessary to maintain surface purity during the cathodoluminescence studies. Performing DRCL at 36 K reduces the thermal footprint in the spectrum and allows for a stronger luminescence signal to noise ratio. TDCL shows the presence of defects in the crystal through hysteresis and will ideally show population filling. A monochromator will be used to analyze the resulting luminescence over a spectral range of 2-6 eV, which encompasses the projected band gap for both thoria and urania.

#### **1.4 Crystals**

The three crystals used in this research are shown both pre-cleaning (Figures 1.2 and 1.5) and post-cleaning (Figures 1.1, 1.3, 1.5). Due to time constraints, the undoped thoria was not photographed pre-cleaning. In all figures, a ruler has been added for scale.

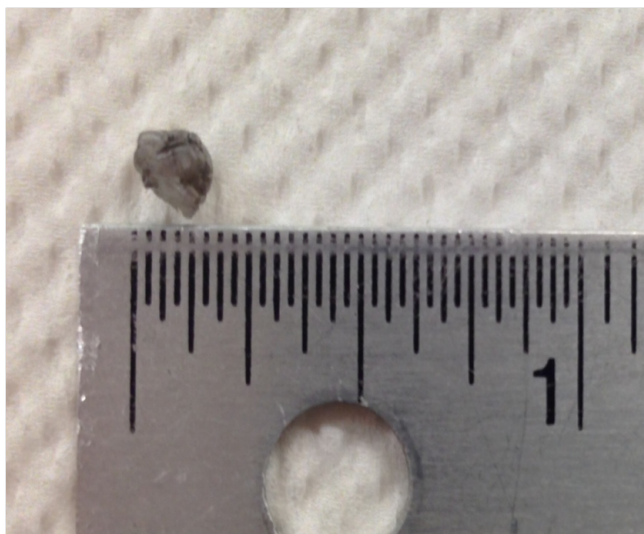


Figure 1.1: Undoped thorium oxide crystal, 001 TO, after chemical cleaning. Post-cleaning mass: 0.3927 g. This corresponds to 500 Å uniformly removed around the cube.



Figure 1.2: Lightly-doped  $\text{U:ThO}_2$  crystal, 003 TU, with uranium mass concentration of 1% before chemical cleaning. Pre-cleaning mass: 0.0027 g.

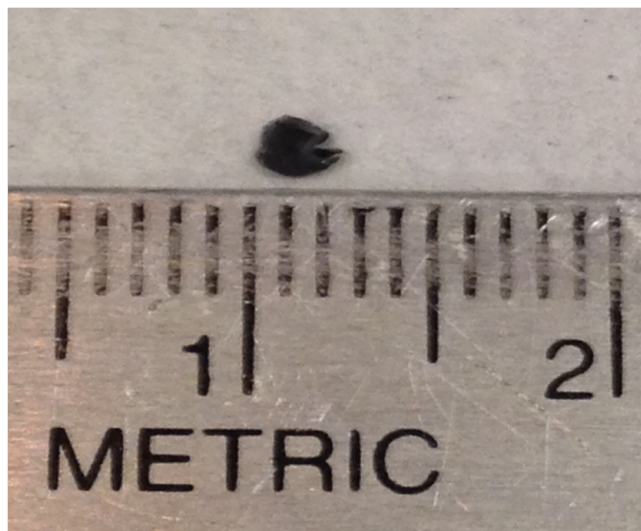


Figure 1.3: Lightly-doped  $\text{U:ThO}_2$ , 003 TU, with uranium mass concentration of 1.08% after chemical cleaning. Post-cleaning mass: .0022 g, which corresponds to  $\approx 50 \text{ \AA}$  uniformly removed around the surface.



Figure 1.4: Heavily-doped thorium oxide crystal, 041 TU, with uranium mass concentration of 22.7% before chemical cleaning. Mass pre-cleaning: 0.341 g.

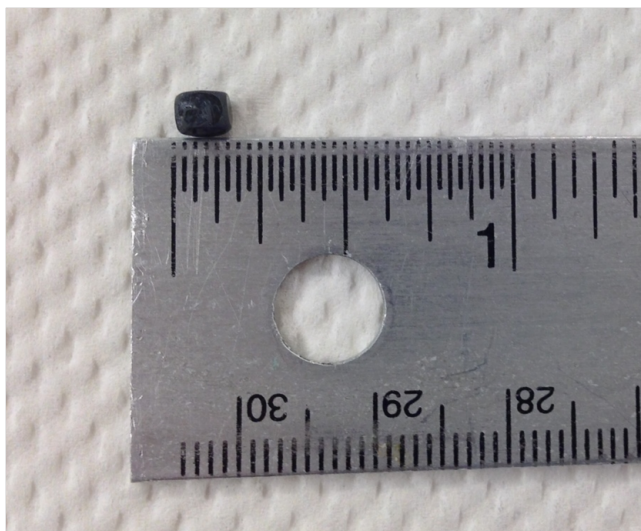


Figure 1.5: Heavily-doped thorium oxide crystal, 041 TU, with uranium mass concentration of 22.8% after chemical cleaning. Rounded edges are as a result of the crystal grinding against the glass beaker. Post-cleaning mass: .3378 g, which corresponds to 750 Å uniformly removed around the cube.

The remaining sections in this thesis are divided into four chapters. First, Chapter 2 details the theoretical background of the material and processes used in this thesis to investigate it. This includes a review of the current standings of research in regards to the materials. Chapter 3 describes in detail the material fabrication, the operational properties of the ultra-high vacuum system used for DRCL and TDCL, the XRF turn-key system, as well as sources of error and the image processing methods used. Chapter 4 displays the data that was acquired in the course of the study as well as proposed explanations for the behaviour of the material. Finally, Chapter 5, summarizes the thesis and gives concluding remarks. The appendices contain a full parts list for the UHV system, CL spectra data, and supplementary CASINO data respectively.

## II. Theoretical Background

This section details the theoretical background behind the materials and the processes used to characterize the material. It begins with an examination of the atomic and electronic properties of thorium, uranium and their oxides. This is followed by an examination of the state of the art of these materials in regards to previous studies performed upon them and where the community stands on their characterization. Next, a detailed discussion of the luminescence occurs with a focus on cathodoluminescence, the primary method used in this thesis. This leads to a treatment on electron interactions in solids. The chapter is concluded with details regarding x-ray fluorescence.

### 2.1 Atomic Properties of $U_x:Th_{1-x}O_2$

Thorium and uranium dioxide are metal oxides with the fluorite crystal structure. The actinide atoms are in a face-center cubic configuration with the oxygen atoms in an interlocking, simple cubic configuration, tetrahedrally bonding to four actinide atoms. These structures share similar lattice constants ( $a_{ThO_2}=5.5 \text{ \AA}$  and  $a_{UO_2}=5.6 \text{ \AA}$ ) and the ionic radii of the two actinide atoms is also similar ( $r_{Th}=1.00 \text{ \AA}$  and  $r_U=1.05 \text{ \AA}$  respectively) [1]. The fluorite structure is presented in Figure 2.1 with the white atoms as the thorium cations and the yellow atoms as the oxygen anions. The oxygen atoms are larger than the actinide atoms due to 5f electron orbital contraction in the actinides causing cations to become smaller while anions increase in size compared to a neutral atom. This results in the ionic radius of oxygen being larger with an ionic radius of  $1.24 \text{ \AA}$  as opposed to the  $1.19 \text{ \AA}$  of thorium and  $1.14 \text{ \AA}$  of uranium [44]. In the lattice, each actinide cation is surrounded by twelve nearest neighbor atoms. There are three atoms per primitive unit cell with an actinide atom located at an octahedral symmetry site and two oxygen atoms at tetrahedral symmetry sites. As a result of this eight-fold metal ligand

coordination (with the actinide and oxygen having coordination numbers of 8 and 4 respectively), an octahedral cluster ( $\text{ThO}_8^{-12}$  and  $\text{UO}_8^{-12}$ ) is representative of the entire crystal. Using extended x-ray absorption fine structure (EXAFS), nearest neighbor distances are found to be 2.42 Å [26].

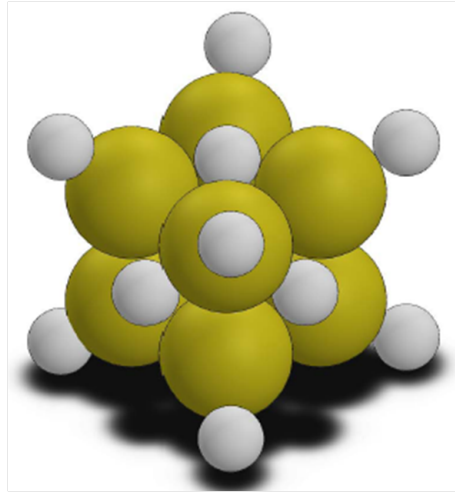


Figure 2.1: Fluorite crystalline structure of thorium oxide.

The minute differences in atomic mass and electronic structure lead uranium to most likely substitute for thorium atoms in the fluorite structure. If the uranium atoms inserted themselves into oxygen positions, large crystalline defects would result due to the size difference between the two atoms causing lattice destabilization. Though even when substitution occurs, thermal conductivity studies show that phonon-lattice strain interaction is increased with as little as 2% uranium [33]. The third possibility is that entire  $\text{UO}_2$  fluorite structures are formed within the crystal rather than a mixed structure. Both uranium substitution and urania formation would result in a Cl peak at the band gap of  $\text{UO}_2$  and a decrease in the intensity of the primary thorium peak.

Thorium has a single oxidation state, +4, when paired with oxygen [4]. In contrast, uranium may be in multiple states, +3 - 6. When a uranium atom takes the place

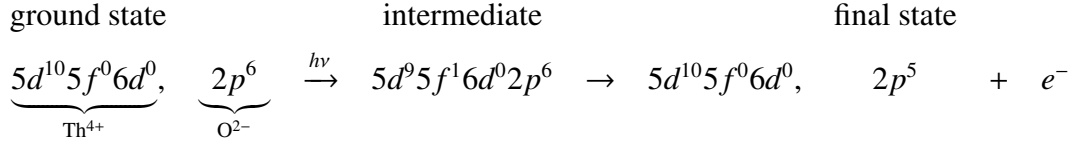
of a thorium atom, oxygen vacancies in thoria can either be filled or an oxygen can be moved to a previously vacant octahedral site. It is expected that  $U^{+4}$  will most commonly replace the thorium atom to allow for electron exchange as has been observed in XPS studies [1]. In order to maintain neutrality, 8 of these uranium ions will be in the +4 oxidation state, and 4 will be in the +5 oxidation state. While the +4 oxidation state of thorium leaves it in the stable radon configuration, uranium loses all of its valence electrons with the exception of the two electrons in the 5f orbital [13]. As is the case with many metal oxides, excess oxygen atoms in the lattice of even a few hundredths of a percent results in the crystal being black under visual inspection. Even after cleaning, the dark coloration was present in the uranium-doped samples. With increasing uranium concentration, the luminescence of the crystals will decrease until the sample is oxygen saturated and  $U_4O_9$  begins to form [43].

## 2.2 Electronic Structure of $U_x:Th_{1-x}O_2$

Thorium is an exception to the Aufbau principle that predicts the electron orbital filling order. Its electron orbital configuration is traditionally regarded as  $[Rn] 7s^2 6d^2$ . The empty 5f orbital exists at lower energy than the 6d orbital but is not always empty. When paired with cubic oxygen, thorium may have electrons in the 5f orbital possibly making its configuration  $[Rn] 5f^1 6d^1 7s^2$  [35]. Theoretical models exist that can predict electron configuration in the valence bands of molecules, such as the spin unrestricted Hartree-Fock-Slater and relativistic Dirac-Slater models. An analysis using these models has been performed in the molecular cluster approximation. The valence levels (Th: 5f, 6s, 6p, 6d, 7s, 7p and O: 1s, 2s, 2p) were examined for  $ThO_2$  and no 5f-character was exhibited [14]. A rectification of these two conflicting viewpoints is proposed in a look at the process by which thorium and oxygen combine.



Table 2.1: A non-hybridization look at the binding reaction of ionized Th & O [11]



In Table 2.1 is shown that prior to the final state of bonding, the 5f orbital in the valence band contains an electron, before depleting and the 5d state filling once again [11]. Adding hybridization does not change the final state, but does alter the intermediate state, including the filling of a 5f orbital detailed by Seaborg [35].

In lieu of these fringe cases, the band structure of thoria is understood to consist of O 2p as the top of the valence band with some Th 6p character present. There is some disagreement as to the conduction band structure. Teterin's calculations show that the conduction band consists primarily of Th 7p and Th 5f character hybridized at the bottom and is joined at higher energies by Th 6d [39]. However, P. Kelly et al conclude that the conduction band is formed primarily of the Th 6d states which hybridize with 5f states to complete the fundamental gap [18]. The Fermi energy exists just above the valence band, and there is no state density at this point. The fundamental band gap occurs between the oxygen 2p state and the thorium 6d state, and its value has been calculated to be 5-6 eV in DOS calculations [18]. Band gap transitions occur in thorium at 4.3 eV as a direct transition at the center of the Brillouin zone and 4.8 eV as an indirect transition at the edge of the Brillouin zone [18]. Quantum selection rules state that for dipoles, holes in a d orbital can recombine with an electron from a p or an f orbital ( $\Delta j=0,1$  or  $\Delta l=1$ ) and  $\Delta l=0$  being spin forbidden.

Uranium has an electron orbital configuration of [Rn]  $5f^36d^17s^2$  in the ground state, with Rn being the electron configuration of radon. Urania is a colored semiconductor, as opposed to the transparency observed in ThO<sub>2</sub> and is strongly

antiferromagnetic [41]. The band structure of urania has not been as extensively characterized as thoria. Unlike thoria, whose Fermi level contains no state density, and lies within the band gap, uranium's 5f band contains the Fermi level and the Fermi energy sits at the bottom of the conduction band [18]. The natural occupation of the two lowest energy subshells of 5f in the ground state of uranium causes the f orbital to exist in the valence band above O 2p with which substantial hybridization occurs [18]. However, because it is an unfilled band, the conduction band retains 5f character as well. In addition, the conduction band contains uranium 6d and 7s orbitals and the oxygen 3s orbital.

The transition between the 2p and 5f in the valence band states is an electric quadrupole transition that occurs at 2.5 eV and as such will be weaker in intensity when viewed using Cathodoluminescence (CL) than the thorium band gap dipole transition of Th 6d to O 2p [46]. The U 5f to O 2p transition occurs when electrons relax from the conduction band to the valence band and a photon is emitted. This small band gap is a result of repulsive interactions causing splitting that occurs between the two highly localized 5f electrons [36] [27]. The 5f to 5f uranium transition from valence to conduction band is spin forbidden and if observed will be much weaker than a  $\Delta l=1$  transition. Further, DOS calculations show two band gap transitions. A direct transition in the center of the Brillouin zone at 4.6 eV is determined as well as an indirect transition at the edge of the zone of 5.4 eV [18]. A separate calculation has the U 7p and U 6d orbitals experiencing hybridization in the conduction band and the fundamental gap between U 6d and the O 2p state is calculated to be 5 eV [23]. As is plain to see, there is contention in literature in regards to the exact band structure of the material from theoretical calculations.

As can be inferred from its smaller band gap, urania is a weak *p*-type semiconductor in contrast to thoria's strong n-type insulating properties. The insulating qualities of thoria can result in charge build-up on the surface when bombarded with

electrons. These electrons then act repulsively towards incoming electrons reducing the incoming kinetic energy of these electrons. This charging effect will result in shifting of the electron beam, and unnatural dips in the intensity of the spectrum due to electrons searching for the easiest pathway into the material.

## 2.3 Previous Studies

A breadth of different studies have been undertaken in an attempt to better characterize both  $\text{UO}_2$  and  $\text{ThO}_2$ . The experimental studies have primarily focused on oxidizing pure actinide crystals (usually powders or thin films) to produce the appropriate actinide dioxide. Using surface oxidized crystals produces inconsistent results because of inhomogeneities in the oxidation process. Single crystals, such as those used in this study, have rarely been studied because of the difficulty required in growing them; yet they are much more desirable because of their consistent structure. The single crystal thorium and uranium oxide studies that have been performed are limited, but provide valuable information about the crystal.

Absorption spectra of single crystal  $\text{ThO}_2$  shows the UV absorption edge at 2632 Å with the start of the absorption peak occurring at 4347 Å [24]. This can be compared to absorption spectra that were taken using mixed powders that were fired into discs. Absorption spectroscopy in the range of 4500-7000 Å, which eschews the primary absorption peak of thoria, shows four different peaks arising across a progressively higher concentration of uranium from undoped thoria all the way to pure uranium oxide. In pure thoria, no peaks are observed in this wavelength range. At 2.5% uranium concentration, there is an absorption peak at 5100 Å and at 6500 Å, with the lower energy peak being more prominent. In the 20% sample, the two that are visible in the 2.5% are joined by a third small peak at 5400 Å [13]. Examining lower wavelengths through electron-spin resonance spectrum and absorption ellipsometry the primary absorption peak for thoria is established at 4000 Å [12, 28].

Due to its nature as an alternate fuel source, most of the investigation into thorium and uranium have been thermal studies. Thermal conductivity measurements have been performed on undoped, lightly uranium-doped and uranium samples ranging from powders to pellets. Polycrystalline solids show a linear thermal expansion coefficient for U:ThO<sub>2</sub> to be  $1.00 \pm .11 \times 10^{-5} \text{ K}^{-1}$  for uranium concentration ranging from 13-91% [1]. These studies show that as uranium doping is increased the thermal conductivity decreases as a result of phonon-lattice strain interactions being enhanced due to the larger size and mass of the uranium in comparison to the thorium [33]. This value for thermal expansion is so small that in the range of 240 K through which the temperature studies are performed, no expansion effects will be seen.

In terms of luminescence studies, a breadth of research has been performed with the most extensive using XPS to characterize the inner valence molecular orbital (IVMO). The inner valence states are those that range from Th 4d to the Th 6p states and O 2s states. The binding energies of these respective states range from 16.5 eV for Th 6p<sub>3/2</sub> to 676 eV for Th 4d<sub>5/2</sub> [40]. These studies showed that the chemical bond between thorium and oxygen molecules is achieved through electrons in the filled Th 6p and O 2s states [40]. From these results, density of states formulations were done on these IVMO that predicted the valence band structures of the material. Other luminescence studies deal with the introduction of a dopant into the fluorite structure. Eu<sup>+3</sup> and Am<sup>+3</sup> have been used as activator ions in luminescence studies on thorium oxide powders, and niobium has been doped into uranium oxide. In thorium, replacing the tetravalent thorium ions with trivalent (three valence electron) Eu and Am results in positive charge compensation. Chemiluminescence was performed on the doped thorium resulting in three principal lines at 5900, 6100, and 6300 Å [4].

Cathodoluminescence studies of undoped thorium were performed in the thesis project of Major Mike Lee at the Air Force Institute of Technology (AFIT), and this thesis

work is the direct follow on to his research. Major Lee acquired spectra taken on undoped thoria pre- and post-TOF-SIMS. TOF-SIMS is the bombardment of local points on the surface of a crystal with carbon molecules to scour off surface layers to look for impurities. As a side effect of TOF-SIMS, localized areas of the crystal were now clean of surface contaminants. Upon inspection under CL, changes in the spectra were seen which provided the motivation to use some form of chemical cleaning used in this thesis to uniformly clean the surface. Pre-TOF-SIMS, Major Lee found large variation in the primary emission peak of  $\text{ThO}_2$ , but post-TOF-SIMS, a stable primary emission peak occurred at  $3037 \pm 11.5 \text{ \AA}$  with no secondary peaks [22]. From this, the absorption edge was determined to be at 5.1 eV. An alternative CL study examined Th that had been oxidized to  $\text{ThO}_2$ . This study showed a single emission peak centered at  $4800 \text{ \AA}$  when examining a Th(533) and Th(111) face under ultra-high vacuum [42].

The source of luminescence in both of these instances was attributed to F-centers in the lattice. Under electron bombardment, an electron can be trapped near an oxygen vacancy post irradiation. In undoped-thoria, there exist a large number of negative-ion vacancies because of the trivalent nature of the impurities in the lattice. These impurities will cause charge compensation to occur in the form of a single negative-ion vacancy (an F-center) every time there are two trivalent impurities. Therefore, under electron bombardment a large number of F-centers are expected with few holes due to the small number of positive ion vacancies [28].

In the literature, CL spectroscopy on  $\text{UO}_2$  has been performed in a limited fashion. Single crystal  $\text{U}_{0.04}\text{Th}_{0.96}\text{O}_2$  studied resulting in two emission peaks at approximately  $3250 \text{ \AA}$  and  $5200 \text{ \AA}$  [6]. No explanation was offered for the source of these peaks nor were clear transition energies established. A second study in the range of  $4000\text{-}7000 \text{ \AA}$  on a uranium crystal that underwent oxidation on various time scales showed a single asymmetrical broad emission peak whose wavelength of maximum

emission occurs at 4700 Å. The peak had a full-width at half maximum (FWHM) of approximately 1500 Å [43]. The beam energy was set at 5 keV which results in mostly surface level (under 500 Å) penetration, appropriate for a surface oxidation experiment. Just as in ThO<sub>2</sub> the peak was attributed to F-center excitation and as the oxidation period increased a continual decrease in the luminescence intensity occurred as a result of oxygen vacancies being filled.

## **2.4 Luminescence Processes in Solids**

In a solid, luminescence occurs as a result of either an electronic transition from a higher energy state relaxing to a lower energy state or to impurities in the structure of the lattice. In a perfect lattice, the quantum mechanical potential is periodic, and as an electron (or hole) travels through that periodic structure any disruptions result in the electron undergoing a change in energy. Impurities in a lattice are called activators and can manifest themselves in multiple ways. In single crystals, the growth process necessitates the use of materials besides just those of the desired crystal; furthermore, any material can not be one hundred percent pure. Impurities in this instance are considered any elements not of the desired elemental type. Impurities can also be an excess of any part of a molecule's desired configuration such as excess oxidation in a ThO<sub>2</sub> crystal. Luminescence can be achieved through photon excitation (photoluminescence), electron excitation (cathodoluminescence), chemical excitation (chemiluminescence) or electric field excitation (electroluminescence). When any of these processes occur, an electron in the host atom will be excited into a higher energy state where it remains according to its atomic lifetime before relaxing, releasing a photon and recombining with a hole.

Electrons in filled or partially filled orbitals form the valence band with the next higher energy levels overlapping to form the conduction band. When an electron is excited into the conduction band, a hole is left behind in the valence band, forming an electron-hole (e-h) pair. When the method of excitation is high energy electrons, such as

from an electron gun, the electrons can generate multiple e-h pairs. The number of these pairs generated per electron is given by the generation factor  $G$ ,

$$G = E_b \frac{(1 - \gamma)}{E_i}, \quad (2.1)$$

with  $E_b$  being the electron beam energy,  $\gamma$  being the fraction of energy loss due to back scattered electrons, and  $E_i$  is the ionization energy [45].  $\gamma$  values can be determined through Monte Carlo simulations and were used to determine the generation factors as seen in Table 2.2.

Table 2.2: Electron-Hole Generation Factors in U:ThO<sub>2</sub> and ThO<sub>2</sub>

Beam Energy(keV)	e-h pairs in ThO <sub>2</sub> (thousands)	e-h pairs in UO <sub>2</sub> (thousands)
2	0.17	0.31
3	0.25	0.46
4	0.34	0.62
5	0.42	0.77
6	0.51	0.92
7	0.59	1.1
8	0.68	1.2
9	0.76	1.4
10	0.85	1.5
11	0.93	1.7
12	1.0	1.8
13	1.1	2.0
14	1.2	2.2
15	1.3	2.3

In order to calculate the ionization energy the equation

$$E_i = 2.8E_g + M, \quad (2.2)$$

with  $E_g$  being the band gap energy and  $M$  is a constant between 0 and 1 eV is used [45]. Using the linear relationship established by Klein gives the ionization energies of thoria as 11.8 eV and 6.5 eV for urania [21]. As is shown, even at 2 keV, 170 e-h pairs are created on average in an insulator like thoria, with almost twice that occurring in urania.

Band structure determines where and how these energy transitions occur with intrinsic processes being those inherent to the host material and extrinsic processes dealing with impurities. E-h pair recombination across the band gap is an intrinsic process that produces a photon equivalent to the energy difference between the bands ( $\Delta E = h\nu$ ). These transitions can be either direct for which no change in electron momentum occurs or indirect which requires a change in electron momentum. Direct transitions are more favorable to occur because only a single particle (a photon) is required for the transition to be made. The change in momentum that occurs as a result of an indirect transition necessitates a phonon which reduces its probability of occurring. The transition is most likely to occur from the bottom of the conduction band to the top of the valence band.

Extrinsic luminescence is a result of factors outside the material properties of the host, such as activators in the solid. When an electron enters the conduction band, both it and its associated hole may move freely through the bands. This combination can form excitons when their Coulombic attraction reduces the difference in their respective energy levels to less than that of the band gap. This is similar to the manner in which localized defects in the lattice produce donor and acceptor sites. Donor sites are regions where impurities in the crystal lattice have a higher number of valence electrons than that of the host solid and therefore introduce additional electrons into the lattice. In a heavily doped material, this creates a localized region where the operational band gap energy is smaller due to the higher valence ( $n$ -type). Acceptor sites are the opposite, where an impurity has



lower valence than that of the host and therefore the conduction band is reduced and more easily accepts electrons (*p*-type). The fundamental band gap, as an intrinsic property of the material does not change, but the operational band gap is an extrinsic property and is subject to changes. These changes come about as a result of donor or acceptor sites, but more commonly are the result of defects in the material which cause band tailing to occur. The full list of these transitions is displayed in Figure 2.2.

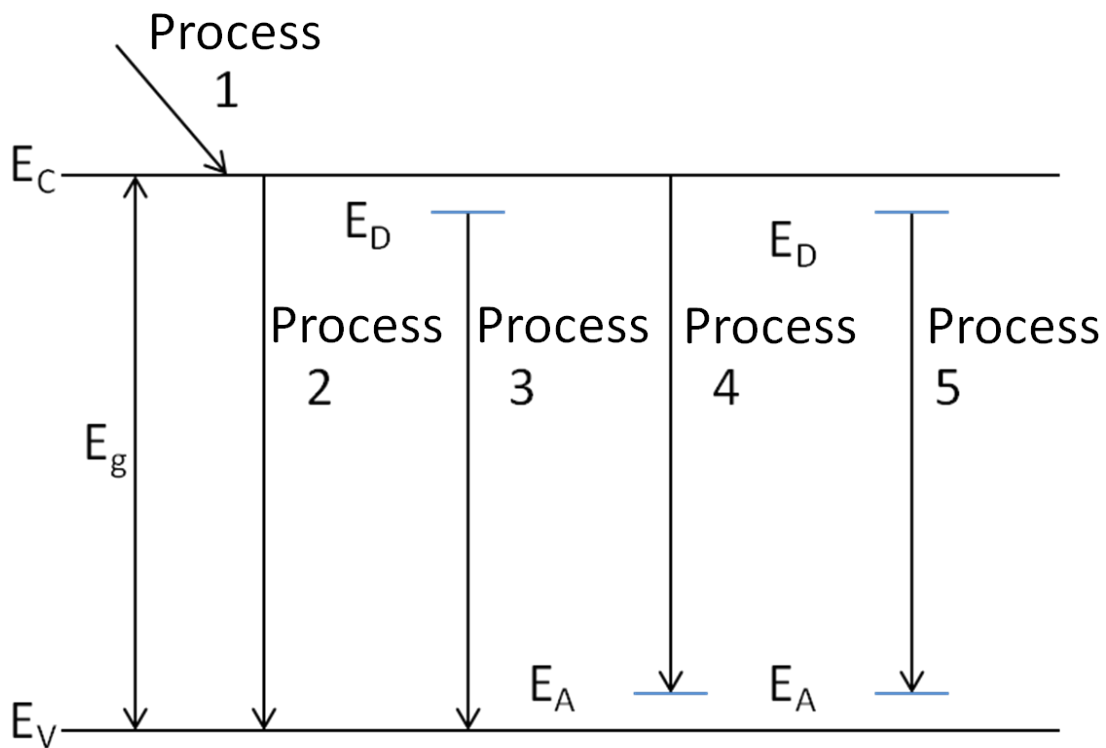


Figure 2.2: Schematic of electronic transitions near the valence ( $E_V$ ) and conduction ( $E_C$ ) bands in a solid including the band gap ( $E_g$ ), donor sites ( $E_D$ ) and acceptor sites ( $E_A$ )

In Figure 2.2, Process 1 demonstrates intraband transitions where the initial energy given to the electron is greater than what is needed to progress across the band and therefore relaxes down through non-radiative (like those described earlier) or radiative

processes depending on the energy needed to reach the conduction band ( $E_C$ ). Process 2 shows e-h pair recombination from the conduction band to the valence band ( $E_V$ ) by releasing photons with energy equivalent to the band gap ( $E_G$ ). Processes 3, 4 and 5, show an extrinsic transition in what is a forbidden region in a pure lattice and is the result of an impurity. The energy of a photon undergoing process 5 is not just the difference in energy between the donor ( $E_D$ ) and acceptor ( $E_A$ ) state. The energy of Donor-acceptor pair (DAP) recombination is found using

$$E(r) = E_g - (E_D + E_A) + \frac{e^2}{\epsilon r}, \quad (2.3)$$

where  $\epsilon$  is the material permittivity, and  $r$  is the distance between the donor and acceptor levels [31]. Similarly, this additional Coulombic attraction term is present in donor site to valence band transitions and conduction band to acceptor site transitions indicating the electrical repulsion felt by the oppositely charged electron and hole.

## 2.5 Depth-Resolved Cathodoluminescence

CL is a method to gather information on short-range interactions, and the characterization of fluorescence centers in crystals. This is the primary means by which this thesis investigates the electronic properties of U:ThO<sub>2</sub>.

In CL, a beam of high energy electrons is emitted from a source and directed onto the sample. These primary electrons from the beam can be divided into two categories once entering the sample: back-scattered and penetrating. Back-scattered electrons on their random walk through the material are eventually ejected back out of the material typically only moving through the surface layers of the crystal. These electrons are ideal for providing information regarding surface uniformity, but give no indication of the composition of the crystal lattice in the bulk and are impossible to detect using the system used in this thesis.

Penetrating electrons interact with the electrons of the material and impart energy and momentum to them in the form of collisions. These electrons interact in methods that are either radiative (photons) or non-radiative (Auger electrons or phonons) processes. Non-radiative processes shape the radiative spectrum, and for small energy transitions, materials will utilize non-radiative methods for relaxation. For large energy transitions, such as across band gap, it is favourable for the material to undergo a radiative transition through the release of a photon [31]. These electrons then impart their energy through collisions to the valence electrons of the materials that form the crystal, which results in the excitation of the electrons. When these electrons relax back down either into donor sites, acceptor sites or the valence band a photon is emitted.

DRCL is an appealing technique for the investigation of impurity and lattice damage defects inside of a material. All comparison experiments are performed using a constant electron beam current; however, by varying the beam energy, the power of the beam can change and result in variable e-h pair production in accordance with Equation 2.1. By keeping the current constant, the relative density of e-h pairs does not change which maintains the level of excitation on the surface of the sample [32]. DRCL is especially useful in looking at fine structure in the form of defects or at layered materials [45]. Oxidized uranium and thorium studies use this technique to examine oxidation depth. For single crystals, the molecular structure should be uniform throughout. However, the solubility rates of thorium are higher than that of uranium, so DRCL can be used to see if these mixed type single crystals do, in fact, maintain homogeneity throughout.

In order to understand a CL spectrum, it is imperative to look at the interaction methods between the electrons and the solid into which they are entering. Inside a solid, electrons are inelastically scattered by other electrons inside of the material. Inelastic scattering is described as an energy loss over a distance as given by the Bethe-Bloch

equation

$$\frac{dE}{dS} = -2\pi e^4 N_A \frac{\rho Z}{EA} \ln \left( \frac{1.166E}{(9.76Z + 58.5Z^{-0.19})} * 10^{-3} \right), \quad (2.4)$$

where  $e$  is the elementary charge,  $\rho$  is the density of the solid,  $A$  is the atomic weight,  $E$  is the electron energy in keV, and  $Z$  is the atomic number [45]. The inelastic scattering of electrons by other electrons gives rise to many different effects: secondary electrons, Auger electrons, x-rays, e-h pairs, and phonons. Of these, only e-h pair recombination results in luminescence in the visible regime with x-rays being too high in energy to be seen. The rest of these are non-radiative processes which can not be directly observed with the equipment used in this study; however they still are important in shaping spectra and are elaborated upon here.

Secondary and Auger electrons are both concerned with non-radiative processes that result in electrons being released from the solid. Secondary electrons are electrons that escape from the material as a result of energy being transferred from the primary electrons (those from the beam) to electrons in the solid. The energy imparted is enough to overcome the binding energy of the electrons in the solid. These electrons then may escape the material. Auger electrons occur when an electron from an inner-shell leaves a hole behind after being excited and an electron from a higher shell drops to fill the vacancy by emitting a photon. This low energy photon or phonon is then absorbed by a second electron, exciting it into the conduction band and allowing it to escape the host atom [45].

Phonons are vibrational modes in an atomic lattice that are quantized into discrete units of acoustical energy. Phonons exhibit wave-particle duality and are subject to the Heisenberg uncertainty relation. When electrons are excited from the valence band to the conduction band in an indirect transition, a phonon can be used to overcome the energy gap and impart the necessary momentum to the electron to make the transition. Phonons are much lower energy than photons, and as such phonon transitions across band gap are highly improbable. Phonons can be used to bring an electron into a donor or out of

an acceptor state. They are also seen in intraband transitions in the conduction band. The highest energy phonon in thorium dioxide is 0.056 eV [15].

The program CASINO is used for modeling electron pathways through solids and is useful in establishing penetration depths for DRCL measurements. The Monte Carlo method uses pseudo-random numbers in order to approximate statistically significant events. In the case of electron beam penetration into a crystal, the electrons undergo several scattering events that result in the randomization of the trajectory. Based solely on the generation factor, electrons from the beam can undergo several thousand scattering events before losing enough kinetic energy to become trapped. The range of these electrons can be found using the Gruen equation

$$R_e = \left( \frac{kE_b^\alpha}{\rho} \right), \quad (2.5)$$

with  $\rho$  being the material density,  $k$  is a value dependent on the atomic number of the material and the beam energy and  $\alpha$  which also is dependent on the atomic number [45]. CASINO uses a modification of Equation 2.4 called the Joy-Luo equation

$$\frac{dE}{dS} = -78500 \frac{\rho Z}{AE} \log\left(\frac{1.166E}{J} + 1\right) (keV/cm), \quad (2.6)$$

where  $J$  is the mean ionization potential,  $\rho$  is the density of the material,  $A$  is atomic weight [17]. Unlike Equation 2.4, the Joy-Luo equation allows for ionizations in low energy orbitals and for energies below 100 eV. This is used to determine both the ionization potentials, necessary for determining the backscattered energy that is used in the generation factor calculation, and the energy loss for each electron due to scattering. A sample CASINO simulation for 22% doped U:ThO<sub>2</sub> is given in Figure 2.3. The blue lines show the electron pathways through the crystal that result in radiative processes, and the red lines indicate back-scattered electrons. The electron trajectories are calculated by having each electron travel in a stepwise manner, with the scattering angle being chosen

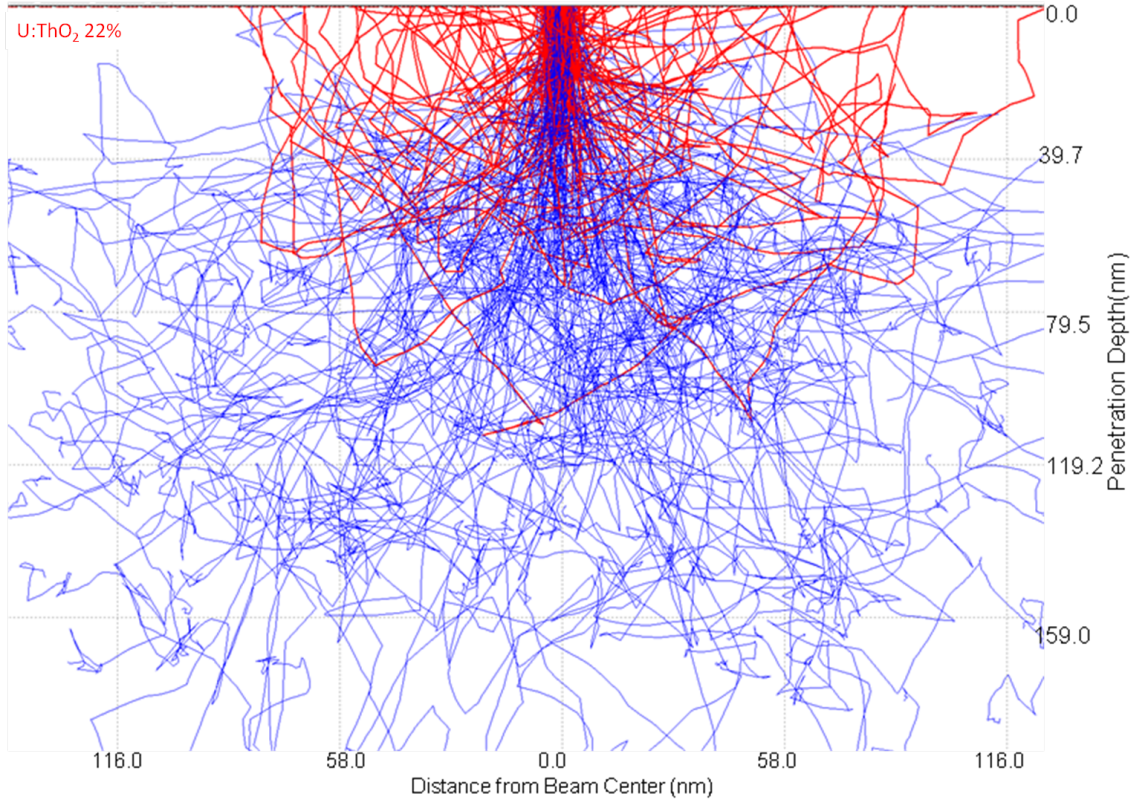


Figure 2.3: CASINO simulation for electron pathways into 041 TU with 7 keV beam energy. The simulation was run using 20,000 electrons and a beam width of 10 nm for the effect of this display. Lines in red are back-scattered electrons and blue lines show non-back scattered electrons.

using a random number generator. In the case of CASINO this is the Press random number generator [34]. The step length between each scattering event is given as

$$S = -\frac{A}{N_A \rho \sigma} \ln(R), \quad (2.7)$$

with  $A$  being the atomic weight in g/mol,  $\rho$  being the atomic density, and  $\sigma$  being the scattering cross section found using Mott elastic scattering cross section.

## 2.6 Temperature-Dependent Cathodoluminescence

TDCL was performed to investigate two properties of  $U_x:Th_{1-x}O_2$ : hysteresis and thermal band gap dependence. As the temperature rises, energy is imparted into the lattice as thermal energy causing the lattice to expand and electron populations to shift in energy levels. This allows for different transitions to be observed than would be seen at low temperatures. Further, the thermal energy causes a reduction in both direct and indirect energy band gaps.

Hysteresis is the dependence of a crystal's current state on its past state. TDCL can be used to investigate this by performing a temperature walk from low to high (or vice versa) and then returning to the original temperature. CL spectra can then be compared between the sample as the temperature was rising and when the temperature was falling to determine if any variations occurred. Defects are very temperature dependent and as such hysteresis is useful for their identification. If a spectra retains its original features, only losing intensity as the temperature increases it can be inferred that it is relatively free of defects. If the transition energy changes in the spectra as the temperature changes this is indicative of defects in the material. Hysteresis changes the previous environment and if the transition energy variation remains constant despite the previous environment, this is another sign of defects. Most commonly defects take the form of Frenkel or Schottky-type. Frenkel defects occur when an atom moves from its stoichiometric position in a lattice leaving a vacancy but, rather than leaving the lattice, inserts itself somewhere else as an interstitial. A Schottky defect occurs when atoms of both species are removed leaving a vacancy of each type.

For TDCL the beam current and voltage was held constant as the temperature was increased. As a result the beam power,  $P=IV$ , was held constant which in turn provided a constant total electron-hole pair injection rate [45].

## 2.7 X-ray Fluorescence

XRF is a technique to determine the chemical composition of a sample. X-rays are photons with energies in the range of 0.125-125 keV and impinge upon the surface of a sample. These x-rays excite electrons from one of three sets of core orbital classifications (K, L or M) based on principle quantum number,  $n$ . K electrons are from low energy orbitals ( $n=1$ ), L electrons are from higher energy orbitals ( $n=2$ ), and M electrons are from very high energy orbitals ( $n=3$ ). Elements with a greater atomic number than cesium do not display K transitions due to their energy being outside the range of the detector [2]. The incident x-rays excite electrons out of one of these three shells and the electron is ejected from the atom. At this point, an electron from a higher shell drops down to fill the vacancy and a secondary x-ray is emitted. A spectrum is then obtained from the emitted radiation. The XRF source is a rhodium filament, and therefore, rhodium is seen in many of the spectrum taken despite no rhodium being expected to be present in the sample.

Being of such high energy, XRF is useful for identifying elements of a higher atomic number (such as Th and U) through K, M and L lines and is therefore ideal for the purposes of determining where in the crystal uranium is found [2]. The XRF can be used to determine mass concentration ratios for the various elements present in the material. Therefore, the XRF spectra is able to be used to determine if the cleaning methodology used in this research worked by examining the the elemental concentrations before and after the cleaning.



### **III. Methodology**

This chapter is broken into six sections which detail the systems and materials used and the operation of all the equipment as well as sources of error. First, the crystal fabrication method is detailed followed by the XRF machine operation which enabled the determination of the chemical composition of the crystals. Then, the cathodoluminescence system design, operation, and sources of error are examined. Finally, the chemical cleaning process which was developed for these crystals is detailed.

#### **3.1 Experimental Approach**

Examination of each of the three crystals was approached in the same manner to ensure consistency in the experimental procedures. First, each sample was examined using XRF to determine its approximate elemental make up. This enabled accurate CASINO simulations for each of the samples to determine the electron penetration depth and the divergence associated with each. Diagnostics were performed on the two electron guns to determine the optimal beam current for the best signal-to-noise (S/N) ratio without damaging the crystal with a high electron fluence and to maintain the longevity of the gun filament. Then, DRCL was performed at 36 K in order to examine the structure of the material from the surface into the bulk. Surface depth is considered by surface chemists to be the top 50 nm of the sample. Simulations showed that for beam energies greater than 4 keV in all samples resulted in an average penetration depth of greater than 500 Å, which is considered to be past the surface of the material.

Measurements were taken from 3-14 keV with four intervals in between (5, 7, 10, 12 keV respectively). This allows a strong determination of the surface structure, transition zone from surface-to-bulk, and the bulk. Following these measurements, TDCL experiments were performed with the temperature raised in 40 K increments starting at 36

K and ending at 276 K. Monte Carlo simulations dictated that 7 keV would be an acceptable beam energy to perform these measurements and see strong bulk interactions, and experiments provided strong signal-to-noise ratios at this beam energy. Following this, the samples were chemically cleaned, and each step in the process was repeated with the exception of the Monte Carlo simulations as these were performed assuming no impurities.

### **3.2 Crystal Fabrication**

Two of the crystal samples (001 TO and 003 TU) investigated were hydrothermally grown single crystals produced by Dr. Michael Mann's group at Clemson University [25]. Sample 041 TU was grown using the same process by Jacob Castilow [6]. None of the samples were grown in the same batch. The hydrothermal method was used due to the high melting point of thorium ( $3390^{\circ}\text{C}$ ), which prevents traditional melts from being used as the temperature is difficult to reach for synthetic purposes [38]. This hydrothermal growth process uses spontaneous nucleation reactions in silver ampoules with thorium powder placed inside. Water was used as counter pressure by filling the remaining volume in the 27 mL autoclave. Pressures were held at 10-30 kpsi. A seed crystal of thorium was used, and the feedstock was .25-1.0 mm spontaneously nucleated crystals combined with 1-2.5 g of  $\text{ThO}_2$ . The mineralizer used was a 6M CsF solution with the thorium saturating in the mixture at  $750^{\circ}\text{C}$ .

The uranium-doped thorium samples (003 TU and 041 TU) were grown in a similar fashion as the thorium crystal. The seed crystal was again thorium. The feedstock powder used in the solution for 003 TU contained 2-5 % uranium by volume as well as thorium, and the solution used for 041 TU contained 40 % uranium by volume and was grown in a 9M CsF solution. XRF measurements were used to investigate if the seed powder achieved the predicted concentration percentage.

### 3.3 XRF System

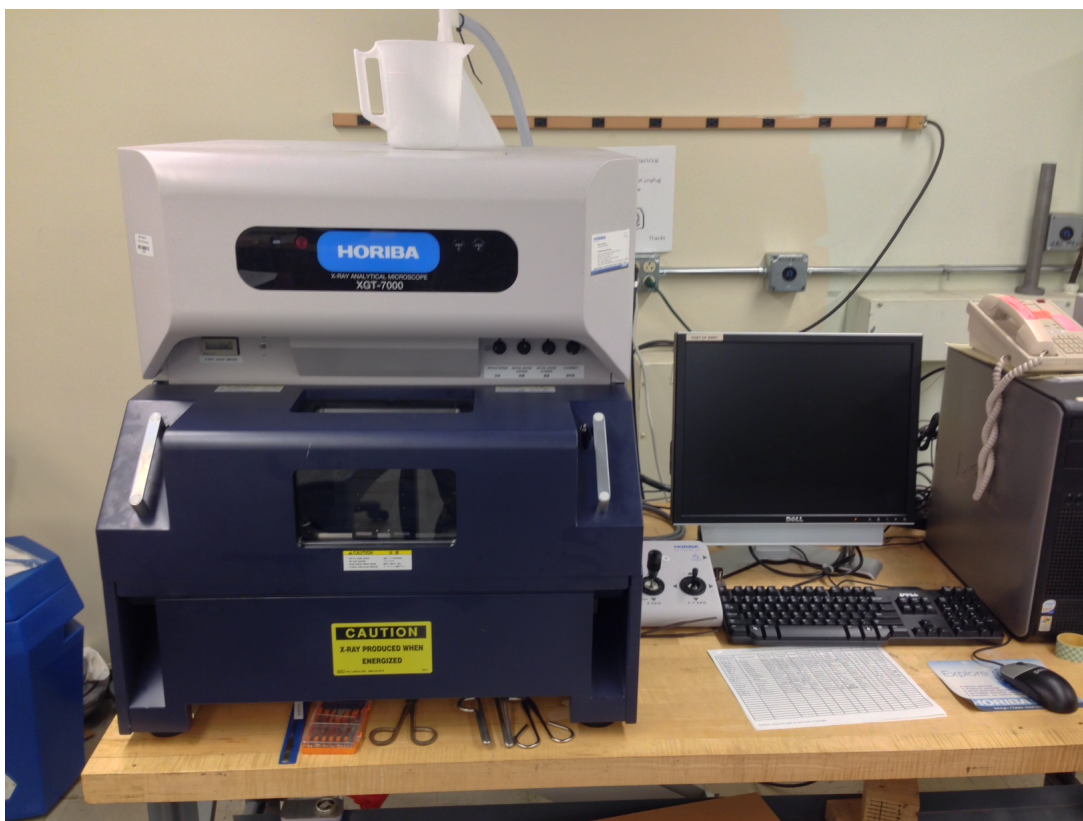


Figure 3.1: Horiba XGT-7000 XRF imaging microscope used to conduct XRF measurements on the three samples pre- and post-cleaning to examine the elemental composition of the samples.

As described in Section 2.7, XRF is used to determine the elemental composition of the crystals. The purpose of this was twofold. First, prior knowledge of substantial impurities could be useful in the interpretation of the CL spectra taken. Furthermore, the uranium-doped crystals have heretofore been uncharacterised and as such the exact amount of uranium found in each of them is unknown. By performing XRF measurements pre- and post-cleaning, the mass concentrations of thorium and uranium should be seen to more accurately reflect their actual concentration as elemental impurities are removed.

XRF was performed using a turn-key Horiba XGT-7000 XRF imaging microscope as shown in Figure 3.1. The machine settings were constant for all measurements. A voltage of 30 keV and an acquisition time of 2000 seconds was used on each of the twenty points. The chosen surface was picked based on which face was considered the smoothest that could also be properly mounted into the CL system. A grid of twenty points was used, allowing for an examination of a large surface area on the face of interest. The aperture of the XRF was set at 100  $\mu\text{m}$  and an average dead time of 20% was observed across all twenty spectra taken. The dead time is the time interval after an electron is detected before the next can be detected. The longer the dead time percentage the less active detection time occurs in a scan. The system has an x-ray detection range for elements from Na to U. A rhodium lamp was used and as such any rhodium lines in the XRF spectrum were regarded as evidence of the lamp's footprint and not evidence of the presence of rhodium in the crystal. Mass concentration percentages were calculated as an average of the elemental concentration in each of the twenty points.

### **3.4 CASINO**

CASINO was used to determine the penetration depth of the electrons into both the undoped and uranium-doped thoria. This gave information concerning the beam energy necessary to see only surface features, a mixture of surface and bulk features, and solely bulk features. This was useful in setting the 7 keV energy used for TDCL studies, as at that energy penetration occurs well into the bulk for all three crystals while also not putting undue fluence onto the crystal or taxing the electron gun. Simulations were run for each sample from 1-15 keV using 20,000 electrons. Average penetration depths were calculated in MATLAB and are displayed in sample CASINO simulations for each sample in Appendix C.

### 3.5 Cathodoluminescence System Design

The cathodoluminescence system used for this thesis was a pre-constructed stainless steel, UHV system. It consists of five parts: the main chamber, the vacuum pumping system, the cryocooler, the electron gun, and the light-gathering components. A full list of the equipment used in the construction of the machine is given in Appendix A.

#### 3.5.1 Main Chamber.

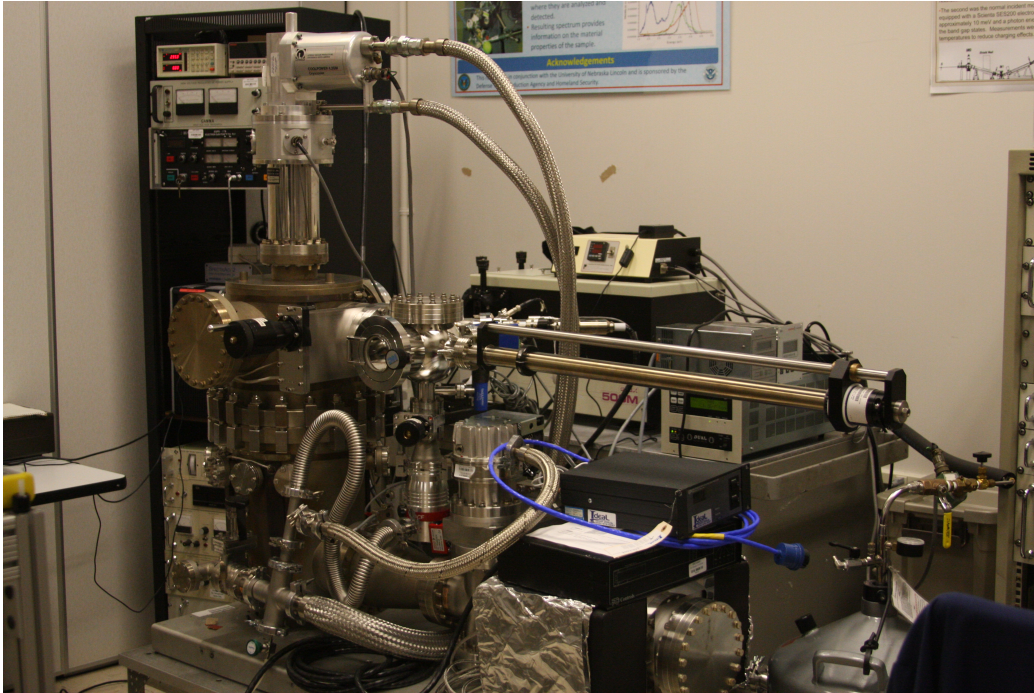


Figure 3.2: Full view of cathodoluminescence system. The main chamber with cryocooler is positioned on the left side of the image. Behind the system on the work bench are the pump controllers on the right side, and the monochromator and PMT housing on the left.

The CL chamber consists of two main parts: the chamber itself and a load lock with loading arm. The chamber is a 76 cm tall, 18 cm diameter, 304-stainless steel cylinder with a sample holder placed in the center of the chamber attached to the cold finger of a He refrigerator. It is positioned at the far left of Figure 3.2 and is labelled as 4

in Figure 3.3. An ion gauge in the chamber can be used to provide the pressure inside the chamber. A glass window on the back of the system provides the exit for photons emitted from the crystal. When samples are mounted on the manipulator arm through the load lock, the main chamber is sealed off via the manual gate valve and dry nitrogen vapor is flushed through the load lock to reduce the introduction of water vapor and atmospheric contaminants. The samples are mounted using strips of tantalum wire spot-welded across the sample face and securing it to a tantalum plate. This plate is then fastened to a copper sample holder on the manipulator arm in the depressurized load lock. From there, vacuum is re-established through the combined use of a scroll pump used to achieve a vacuum pressure of  $10^{-2}$  Torr and a Pfeiffer turbo pump to bring the load lock to  $10^{-5}$  Torr. The sample is then inserted into the main chamber where it is locked on the sample mount facing a quartz viewing window with the electron gun at an angle of thirty degrees to the crystal in the plane of the sample holder.

### **3.5.2 Vacuum Methods.**

Ultra-high vacuum is necessary for CL experiments in order to prevent surface contamination while the experiment is being performed. To obtain UHV, two different processes are used: an extensive pumping system that consists of four pumps and system bakeout using heating tapes.

The system consists of a dry scroll pump, two turbo pumps, and a vacion pump. The TriScroll 600 series Dry Scroll vacuum pump is a mechanical pump that uses two interlocking spirals that rotate compressing the gas and drawing it out of the chamber. The scroll pump operates in the range of 760 –  $7 \times 10^{-3}$  Torr pumping at 500 L/min when operated at 60 Hz. This pump is used any time any part of the system is brought to atmospheric pressure. From here, two turbo pumps are able to handle the vacuum regime of  $10^{-2}$  –  $10^{-5}$  Torr. One is a HiPACE TurboDrag Pump from Pfeiffer and the other an Agilent turbo-molecular pump. The turbo pumps operate using a high throughput fan

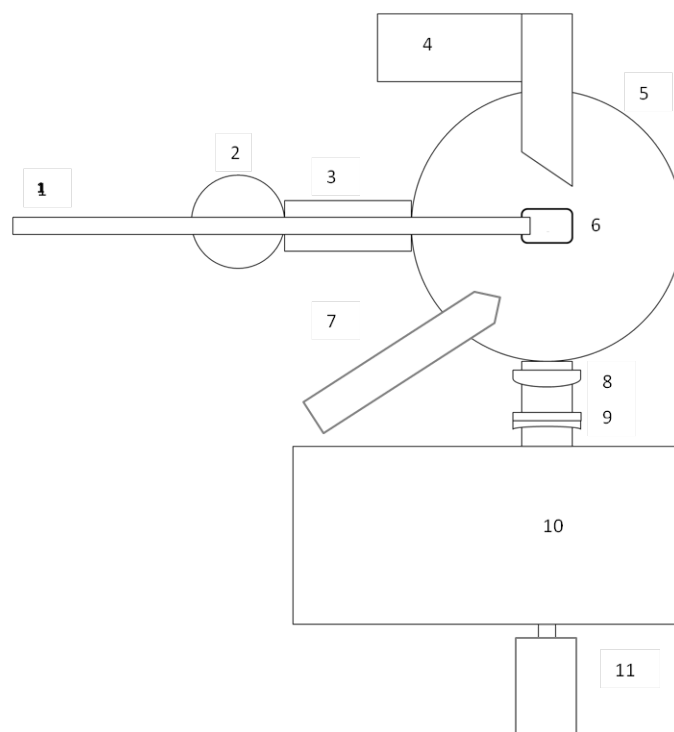


Figure 3.3: Schematic of cathodoluminescence system. 1) Manipulator arm 2) Load lock 3) Manipulator arm pass through 4) Cryocooler 5) Main chamber 6) Sample mount 7) Electron gun 8) Collimating lens 9) Focusing lens 10) Monochromator 11) PMT.

spinning at 250 – 750 Hz that pulls particles into the rotor in accordance with Bernoulli's principle. The Agilent pump is used when the entire chamber is exposed to atmosphere such as after baking occurs, or when the cooler out-gasses as a result of activation of the heater. In that instance, the Agilent pump is used to back up the vac-ion pump. The Pfeiffer pump is used principally when samples are exchanged and just the load lock needs to be pumped down.

The final pump is an 300L Varian vacuum ion pump which uses two high voltage plates that result in an ion producing discharge. These ions sputter titanium surfaces that release titanium particles into the system. The titanium has a high sticking coefficient, except with respect to the noble gases which have to be completely buried by titanium

molecules. These molecules then essentially become a part of the chamber wall resulting in a net pumping action. This burial effect is useful for inert gases, especially H<sub>2</sub>, He, Ne, and Ar.

The chamber and connections are non-magnetic stainless steel which contains hydrogen, nitrogen, and carbon oxides that are dissolved into a metal during melting and casting [29]. By heating the chamber and connections, the metal expands and a portion of the trapped gases are released allowing the pumps to remove the atoms from the system. The stainless steel chamber had previously undergone multiple sandblasting and high temperature bakes in order to render the interior clean and outgassed. In order to reduce the gas load in the system, the chamber and connections are uniformly wrapped with heating coils and brought to a temperature of 180 °C. Since the chamber and connections have already been treated at high temperatures only this low temperature bake is necessary.

### **3.5.3 *Cryo Cooler.***

In order to conduct TDCL and improve signal-to-noise ratio, the chamber uses a Leybold CoolPower 4.2 CGM liquid helium circulation cryocooler to control the temperature of the sample holder and sample inside the main chamber. As thoria is an insulator, it is important for the sample to have a large contact area with the cold finger. Through conduction, the sample can hopefully be brought to the same temperature as the finger. The temp is controlled and displayed using a LakeShore 330 autotuning temperature controller. For the majority of DRCL performed, the chamber was brought to its coolest temperature, 36 K. This temperature is allowed an average of twenty minutes to stabilize prior to measurements being taken. The cold finger is cooled prior to injecting the sample into the cold finger as the cold temperatures draw particles to it. By delaying the insertion of the sample onto the cold finger, surface contamination is reduced. Unless otherwise stated, all CL measurements were taken at 36 K. For TDCL, the cooler, working in conjunction with a built in heater, allowed for forty degree increment steps to be taken.



### 3.5.4 Electron Gun.

The electron gun used for the majority of the experiments is a Kimball Physics EMG-12 electron gun with a barium oxide cathode and a thoriated tungsten filament. The original electron gun was a Kimball Physics EMG-12 electron gun with a tantalum cathode. Spectra from this gun will be explicitly labelled as from the original gun, otherwise all mentions of electron gun will be in reference to the gun with the barium oxide cathode. Both guns were controlled using a Kimball EGPS 12B power supply. The beam is produced by a triode and controlled through the use of deflection and focus. A schematic of the electron gun is provided in Figure 3.4. The triode operates using a

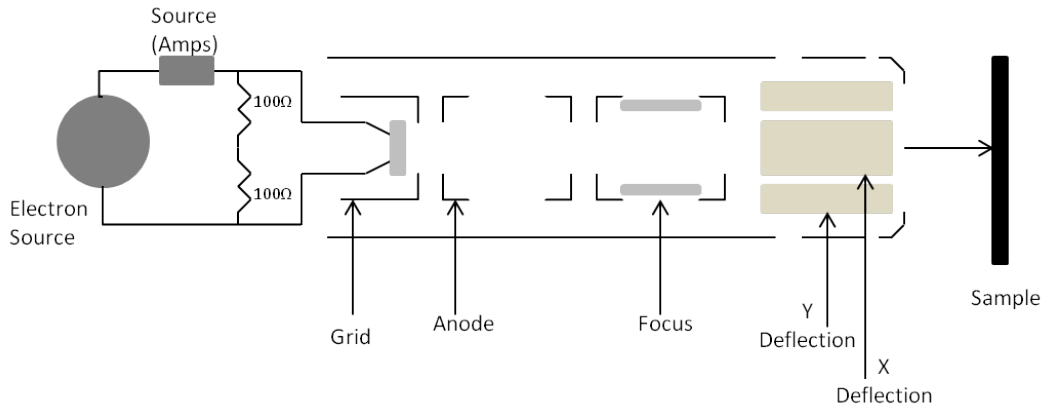


Figure 3.4: Schematic of electron gun

cathode, grid, and an anode. The cathode is mounted on a heater labelled in the schematic as the electron source. As the temperature rises, electron emission occurs in two regimes: a temperature limited mode and a space charge limited mode. Emission in the temperature limited mode is governed by the Richardson-Dushman equation

$$J_e = A_e T^2 e^{\frac{\phi}{k_B T}}, \quad (3.1)$$

where  $J_e$  is the emission current density in amps/cm<sup>2</sup>,  $A_e$  is a constant 120 amps/cm<sup>2</sup> K<sup>2</sup>, T is the cathode temperature in Kelvin,  $\phi$  is the work function of lanthanum hexaboride, and  $k_B$  is Boltzmann's constant [20]. Emission in the space-charge limited mode is governed by the Langmuir-Child equation

$$J = 2.335 \times 10^{-6} V^{3/2} / d^2, \quad (3.2)$$

where  $J$  again is the emission current density in amps/cm<sup>2</sup>,  $V$  is the high energy potential applied to the cathode in volts, and  $d$  is the distance between the anode and cathode in cm [20]. The electrons are then accelerated by the electric field produced by the triode. The grid is a structure within the cathode through which an applied voltage produces an electric field to suppress the edges of the electron beam leaving only the electrons from the cathode center to be emitted. Finally, the ground potential anode is necessary to create the electric field that guides the electrons' trajectory. The beam can be manipulated using the focus and the deflector. The focus uses two grounded tubes with a third tube between them that applies a focusing potential in order to broaden or narrow the beam. The deflection is a system of two pairs of plates that are placed past the focus in the gun. Electric potentials are applied which cause the beam to curve and deflect in accordance with manual inputs by the user. As shown in Figure 3.5, the electron gun is mounted directly on to the main chamber. Beam energies are variable from 0.50-20.0 keV, though only the range of 2-16 keV was utilized in this study. Two different electron guns were used with the original gun using a source current of 2.3-2.4 amps. The original gun was a similar model with the only difference being the elemental composition of the cathode, that of tantalum rather than BaO. The filament on this gun failed and so the replacement gun with the BaO cathode was used. The replacement gun's operational source current was 1.6-1.65 amps. In order to maintain consistency with the original gun whose required source current was substantially higher, the electron current through the Faraday cup was matched. In order to read the current through the gun, a Keithley 6458 picoammeter was

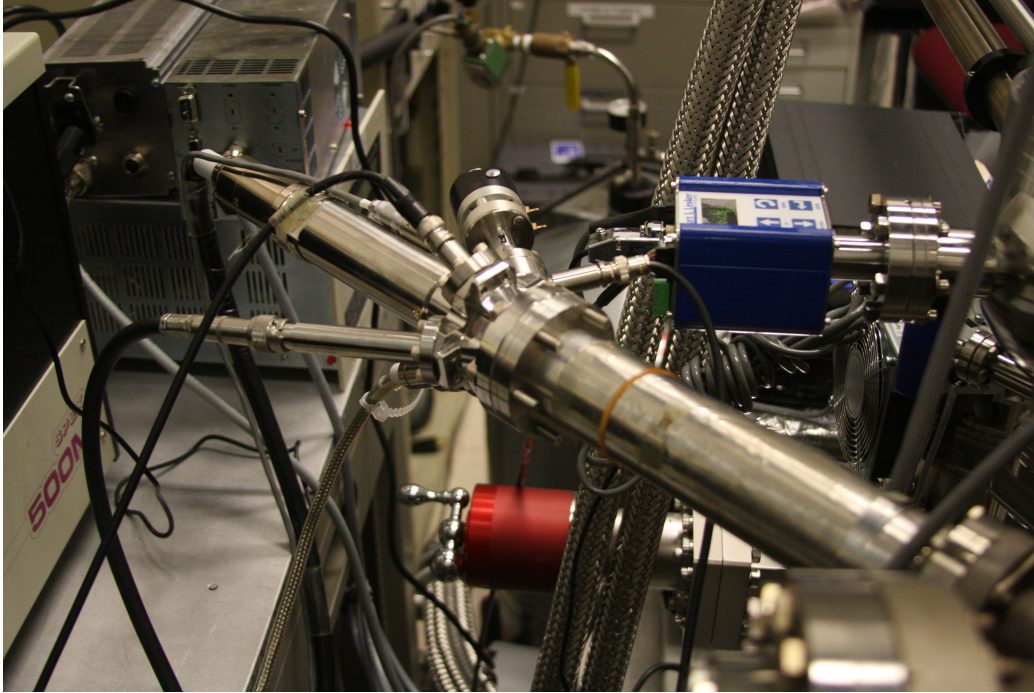


Figure 3.5: Kimball Electronics electron gun used in the cathodoluminescence system. Gun is oriented such that the beam strikes the sample at 30 degrees.

connected to the electron gun. This current is in the range of 5-25  $\mu\text{A}$  dependent on factors such as the temperature of the chamber and the beam energy.

After exiting the gun, the beam of electrons hits the sample causing excitation. As the electrons in the crystal relax, photons are emitted which diverge hemispherically outwards hitting the viewing window. Past the viewing window is a series of two open air optics followed by the monochromator and the photomultiplier tube (PMT)

### 3.6 Optics and Monochromator

As the photons travel out of the vacuum system and into the atmosphere, they reach two lenses. First, a 30 cm planoconvex focal length glass collimating lens was chosen as its focal length is the distance from the exit window to the location of the crystal on the sample holder. The light is focused through the lens into a column that travels to a

15 cm focal length planoconcave glass focusing lens. This second lens meets the f number (the ratio of the lens' focal length to its diameter) of the spectrometer which is important so as to neither over or under fill the spectrometer grating. The saturation that results from overfilling will drastically reduce the S/N ratio. Underfilling the grating reduces the resolution possible with the grating. These optics guide the photons from the chamber into a Spex 500 M monochromator. From there, the beam passes into a Products For Research, Inc, photomultiplier tube (Serial #19941-95) and detector.

As the photons travel from the crystal through the second lens they are focused into the entrance slit of the Spex-500 monochromator. Once inside the slit, the light is reflected off two mirrors before reaching the blazed grating, the ridged surface at the center of the monochromator seen in Figure 3.6 which is blazed at  $3000 \text{ \AA}$ . The grating

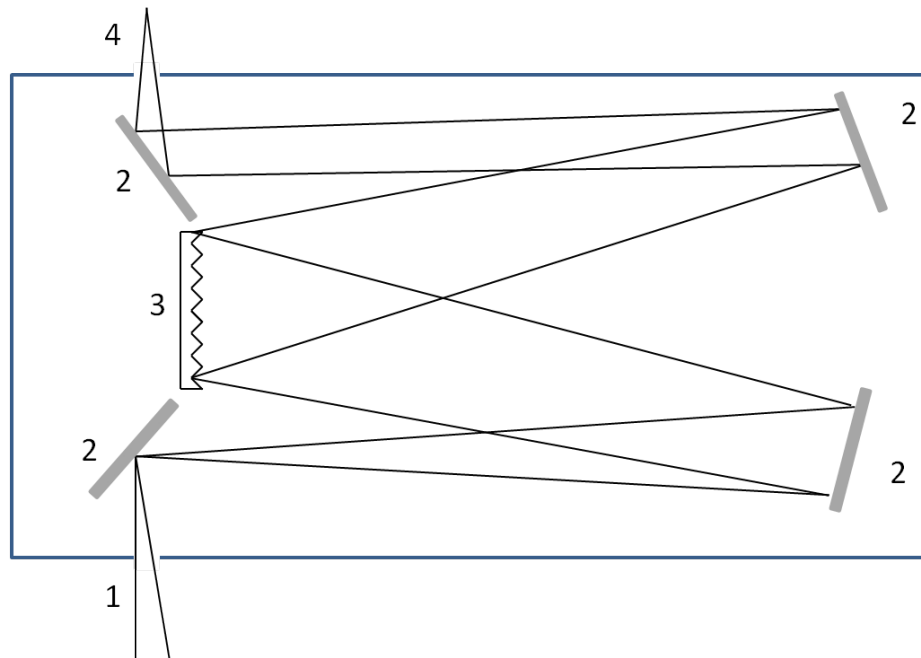


Figure 3.6: Schematic diagram of photon pathways through monochromator. 1) Entrance slit 2) Mirrors 3) Grating 4) Exit slit

is blazed to shift the energy away from the zeroth order reflection to the first order. As the grating rotates, different wavelengths are allowed through as the light is reflected at different positions on the mirrors. As the light leaves the exit slit, it enters the PMT. The PMT creates an electrical current proportional to the number of photons entering, thus amplifying the signal. The PMT is necessary in order to produce a good S/N ratio. The PMT was operated at -1200 V.

### **3.7 Signal-To-Noise Ratio Improvement Techniques**

In spectroscopy, the struggle to acquire a stronger S/N ratio is paramount. In order to improve the S/N ratio several parameters could be manipulated both on a system and on a software level. On a system level each time a new spectrum is taken, four parameters are adjusted in order to acquire the maximum S/N ratio. First, the position of the beam on the crystal is adjusted using the X-Y deflector. This allows for placement at certain positions to maximize the crystal luminescence. Alternatively this can be used to precisely examine different positions on the crystal to look for inhomogeneities in the structure. Second, the position of the focusing lens is adjusted parallel to the load arm. This is necessary especially when a new sample is inserted into the system as samples are not mounted at precisely the same location. This is then necessary to ensure the radiated photons are focused properly into the aperture on the monochromator. Thirdly, the focus and grid of the electron gun are adjusted. Typically the beam is focused to a small point, no more than a millimeter; however, for some samples a large surface area being covered by the beam provides a stronger signal than a single point receiving maximum fluence. The grid applies a bias voltage to two plates creating an electric field which then causes the beam to narrow at the price of reduced signal. Finally, the slits on the aperture of the monochromator are opened wider to allow for increased signal. For all these studies, the slits were opened to 500 micrometers to minimize the amount of differentiation between spectra. This allows for a resolution of approximately 0.2 Å.

On a software level, the Synerjy program, which controls the spectrometer and is discussed in further detail in Section 3.10, allows for two changes to be made in the acquiring of spectra that alter the S/N ratio. First, the integration time, the time the monochromator sits on each wavelength increment, can be changed. Longer integration times result in a greater amount of signal to be received by the detector. The trade off is that the time required for each scan makes long integration times impractical. For this study, unless otherwise explicitly stated, the integration time on all scans was set at 0.1 s. The step size can also be adjusted in order to increase the resolution of the image, though this again comes with a heavy time cost. Due to the large wavelength range that was viewed in these experiments (2000-8000 Å), a 0.50 Å step was determined to be sufficient to provide the necessary resolution to see detail without sacrificing the ability to take repeat measurements due to time constraints.

### **3.8 Sources of Error**

#### ***3.8.1 Filament Spectrum.***

The filament of the electron gun produces a thermal black body spectrum while the electrons are burned off of the filament. To account for this, the beam was focused off the sample onto the holder itself and the beam energy was reduced to 0 keV. Background spectra for each gun were taken at its respective operating source current (2.4 and 1.63 amps respectively) at 36 K. These background spectra were then subtracted from each of the spectra presented in this thesis. The background spectra not only shows the spectra for the filament but also gives the fingerprint of the thermal environment in which the detector is housed. Therefore, not only are the filament spectra being taken into account, but also the thermionic emission within the photocathode of the detector caused by the environment. Each background spectrum is in Appendix C.

### **3.8.2 Temperature.**

The temperature of the sample was taken using a temperature controller that was connected to the cold finger, but did not directly measure the temperature of the crystal. In order to know the temperature of the sample, a thermocouple would need to be inserted into the chamber, which was not able to be performed using the current experimental design. In order to maintain the integrity of the temperatures measured, as the temperature was changed, the sample was allowed twenty minutes for the temperature of the cold finger to equilibrate.

### **3.9 Cleaning Process**

As a metal oxide, thoria and urania will oxidize under atmospheric conditions. As a result, extensive surface contamination by atmospheric elements occurred on the samples studied in this research. Various methods for producing clean surfaces exist that involve surface bombardment by ions such as sputtering where argon ions are used under vacuum to sputter the surface. In a previous thesis using 001 TO, TOF-SIMS was used to investigate the surface composition. TOF-SIMS uses a pulsed ion beam of Cs or Ga in order to dislodge surface material for study. Following TOF-SIMS, CL experiments were performed and large variances were documented between the pre- and post- spectra. This prompted the development and implementation of the chemical cleaning process used on the three crystals by Dr. David Turner. This process uses a solution of a 18-crown-6 ( $C_{12}H_{24}O_6$ ) and 15-crown-5 ( $C_{10}H_{20}O_5$ ) ethers and picric acid  $C_5H_3N_3O_7$ . In the solution, each of the components performs a specific function. The crown ethers remove alkali cation contaminants while the picric acid is used as a counter-ion so that in the organic phase, the solubility is retained [7, 10, 30]. Acting together, the solution strips the outer surface uniformly of between 500-1000 Å of material effectively removing the entire surface layer.

During the cleaning process, the crystal's weight was recorded before and after in order to determine the amount of surface contaminants removed during the process both in terms of mass and volume. In separate vials, 18-crown-6 solid crystals and 15-crown-5 liquid were dissolved in the solvent dichloromethane ( $\text{CH}_2\text{Cl}_2$ ) which were subsequently mixed through vigorous stirring. Picric acid, which is stored under a layer of water to reduce sensitivity to shock and heat variations, was dissolved in a third vial with ultra-pure water (18M $\Omega$ ). After the solutions were mixed separately, they were combined together (Figure 3.7).

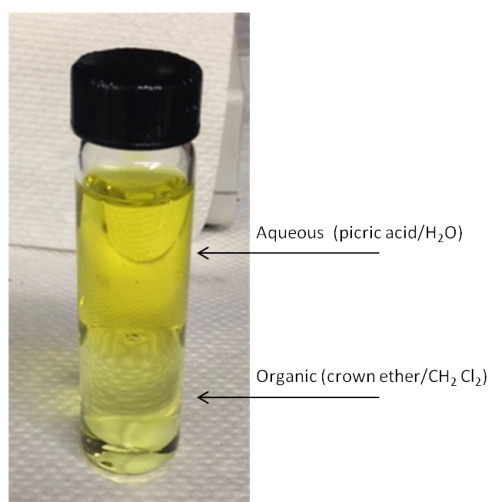


Figure 3.7: Crown ether-picric acid solution with 003 TU crystal inside the vial. A magnetic stir strip was placed in the vial with the crystal to ensure maximum surface area coverage by the solution.

The concentration of the crown ethers and picric acid were determined based on the desire to remove 50 nm from the surface of the 001 TO crystal, for which the protocol was developed and subsequently adapted for the uranium-doped samples. The crystal growth mineralizer for the crystals was CsF, so this solution was chosen specifically to



remove Cs from the crystals. The values for the concentrations of each of the separate solutions are in Table 3.1.

Table 3.1: Concentrations of Cleaning Solution Reactants

Crystal	15-crown-5	18-crown-6	Crown Ether Sol.	Picric Acid	Picric Sol.
001 TO	0.033g	0.040g	15 mM	0.052g	11.3 mM
003 TU	0.033g	0.040g	15 mM	0.052g	11.3 mM
041 TU	0.066g	0.080g	30 mM	0.104g	22.6 mM

All crown ether solutions were in 10 mL of  $\text{CH}_2\text{Cl}_2$  and all picric acid solutions were in 10 mL  $\text{H}_2\text{O}$ . After the crystal and a magnetic stir bar were added, the sealed vial was placed on a magnetic stir plate that kept the crystal active in the solution allowing all faces to undergo the cleaning process. The 001 TO crystal was cleaned over the course of two sessions of 16 hours in the solution. The smaller crystal, 003 TU, was cleaned in a single session of 16 hours in the solution. Due to concerns that the entire crystal might be dissolved in the process, the crystal was monitored while immersed. 041 TU was immersed for 22 hours and the doubled concentration of the solutions was due to its much larger size. 001 TO was less contaminated than the other two samples as it had been cleaned once already and therefore was immersed for the same 16 hours as the 003 TU despite its size similarity to 041 TU. After the crystals were removed from the solution, they were washed using dichloromethane and placed in a vacuum desiccator. The desiccator was filled with a thin layer of drierite that had already been baked. The crystal was placed in a beaker to separate it from the drierite and avoid the deposition of calcium chloride on the surface. The desiccator was pumped down using a scroll pump to  $10^{-2}$  Torr and wrapped in heating coils bringing it to  $180^\circ\text{C}$ . This process dried the crystal out and removed any hydrocarbons that could be trapped on the surface from its immersion in

the solution. The crystal remained in the desiccator for a time equal to its immersion in the cleaning solution. Afterwards, all measurements taken prior to the cleaning were repeated.

### **3.10 Software**

Several pieces of software were used in this study to assist in the gathering and interpretation of data. For cathodoluminescence, the computer used a spectroscopy software package from Horiba called Synergy. This program allows for the manipulation of multiple parameters related to data collection as well as extensive data interpretation tools. In acquiring spectra, the relevant parameters are the wavelength range upon which data is taken, the integration time, and the step size taken by the monochromator. In order to determine the appropriate focus, position and lens calibration to ensure the best S/N ratio, the program is set to preview mode and the monochromator set to the wavelength of maximum emission. Synerjy is placed on continuous run inside preview mode and the three manual parameters are adjusted until the maximum intensity is acquired. All data was exported from this program into MATLAB where all the image processing took place, including standard deviations, averages, and peak emission wavelengths. All graphs displayed in this document were produced using MATLAB. Deconvolutions were performed using a program called Peak Fit through which Gaussian peak fitting was performed.

## **IV. Results and Analysis**

This section covers all the processes used to characterize the crystals. First, the elemental mass concentrations of the crystals was determined using XRF. Then, CASINO simulations were run to determine penetration depths of the electrons from the electron gun into each respective crystal. Next, depth-resolved cathodoluminescence measurements for each of the crystals pre- and post-cleaning were performed and the results were analyzed. Finally, temperature-dependent cathodoluminescence studies were performed for each of the crystals pre- and post- cleaning and the results were analyzed.

### **4.1 XRF**

Prior to any cathodoluminescence being done on the crystals, the quality of the crystals needed to be determined. This was done by performing XRF and looking at the elemental mass concentrations in the material. Specifically, the mass concentration of uranium needed to be known to determine how well the crystal growth process and the cleaning process worked. The XRF machine used was a turn key system whose operational parameters are detailed in Section 3.

The XRF machine operates by focusing the x-rays from the lamp onto specific points on the surface of the sample. Figure 4.1 shows a grid of twenty such points laid out onto the surface of 041 TU prior to cleaning. The lamp focuses on the spot for a set amount of time before the platform the sample is mounted on moves allowing the lamp to focus on the next point. For each of the samples, the twenty point grid used was placed at the center of the chosen face of the crystal far from the edges. For the best CL results, the most planar face was chosen for all measurements. The darker regions are the parts of the face where the surface is uniformly planar and the lighter region in the top left corner is damaged and has inconsistent surface flatness. The cross-hairs show the current position

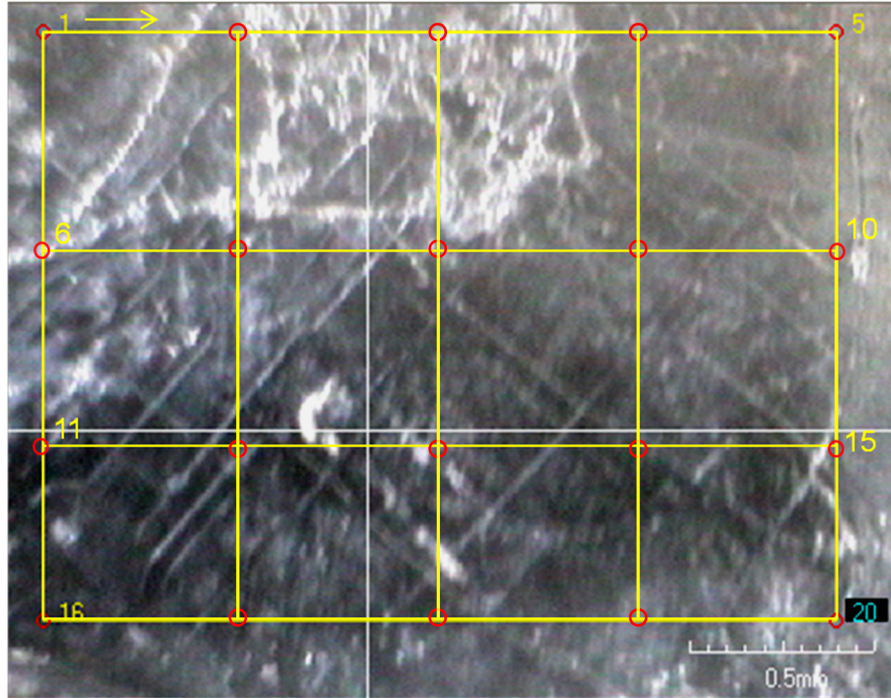


Figure 4.1: Demonstration of 4x5 point XRF grid on 041 TU on which XRF was performed using the Horiba XGT-7000.

where the lamp is focused. This image was taken prior to the start of the scan. The spectra for each of the points was taken and elements were identified using the software package provided by Horiba called Microanalysis Suite- Issue 17b. This produced a list of elements that could be positively identified in the sample, and from the intensity of the spectra the software gave mass concentrations as in Figure 4.2 for 003 TU.

The sample spectra shown is from one of only four points that were identified as having uranium present in 003 TU, unlike 041 TU in which uranium was present at every point the XRF machine sampled. This indicated the small concentration of uranium in the lightly-doped sample. Furthermore, by examining where on the grid the points were located, it was determined that the uranium in the sample followed two distinctly curved lines along the contour of the wedge-shaped sample. This led to the conclusion that not

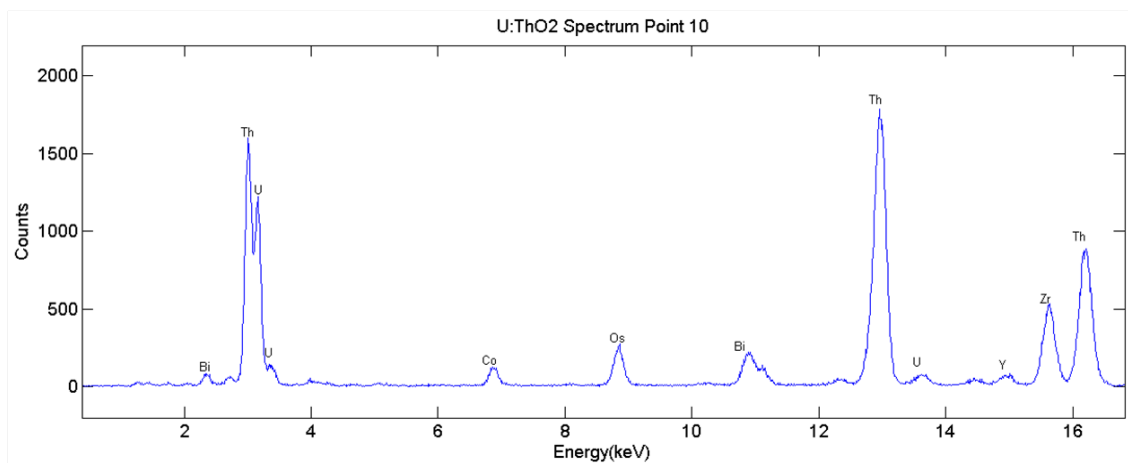


Figure 4.2: Elemental analysis spectrum from point ten of a twenty point XRF grid for 003 TU.

only was the uranium not uniformly distributed through the sample, but that it had grown in a layer between layers of thorium oxide. This shows that this crystal is not of the same quality as the other two in terms of the uniformity of its structure. In both uranium-doped crystals,  $L\alpha$  and  $M\alpha$  lines for both thorium and uranium were visible with uranium's lines at 13.6 keV and 3.16 keV respectively, and thorium's lines at 13.0 keV and 2.99 keV. To acquire an accurate picture of the concentration of all elements present, the mean mass percent concentration of each element across all twenty points was taken and presented in Table 4.1. Results are adjusted for the removal of rhodium from the results.

#### ***4.1.1 XRF Results for 003 TU.***

Table 4.1 provides evidence of either surface contamination or crystalline impurities in the form of ten other elements besides the expected thorium and uranium. Elements with atomic numbers less than eleven, such as oxygen, are not able to be identified by this system. Of the visible elements prior to cleaning, unsurprisingly, thorium had the largest mass concentration by percent at 91.1%. The next most prevalent element was bismuth, which is a common by-product of thorium reactions and exists in

Table 4.1: Mass Percentage Concentrations Pre- and Post-Cleaning

Element	Line	Pre-Cleaning 003 TU	Clean 003 TU	Pre-Cleaning 041 TU	Clean 041 TU
Mg	K	1.86	-	-	-
Si	K	0.097	0.135	-	-
Cr	K	-	-	-	1.09
Fe	K	0.356	-	0.038	0.017
Co	K	0.545	-	-	-
Ni	K	-	-	1.45	0.172
Zn	K	-	0.649	-	-
Ga	K	-	-	-	0.829
Se	K	-	-	0.143	-
Y	K	0.660	0.502	0.767	-
Zr	K	0.214	-	-	0.149
Tc	K	0.086	0.377	-	-
Cs	L	0.117	-	0.822	-
Tm	L	-	0.341	-	-
Yb	L	-	-	-	0.769
Lu	L	-	-	0.160	-
Os	L	0.291	-	-	-
Au	L	-	-	0.619	-
Bi	L	3.12	-	-	-
At	L	-	-	0.216	-
Rn	L	-	-	0.203	-
Fr	L	-	1.08	-	-
Th	M,L	91.1	94.3	72.7	73.2
U	M,L	0.020	1.08	22.7	22.8
Other	-	0.989	1.53	0.182	0.974

quantities of 3.12% mass concentration. Most surprisingly, was that the XRF showed a

significantly smaller amount of uranium doping than was expected to be present in the crystal at only 0.02% uranium mass doping in comparison to the expected 2.0%.

After cleaning, several interesting things were observed. First, seven elements were completely removed from the crystal by the chemical cleaning accounting for a total percentage of 6.5% including all of the bismuth and cesium. In the crystal growth, CsF was used as a mineralizer. As a result, the cleaning process was developed specifically to remove Cs from the crystals, and its removal boded well for the success of the process. Due to these large elemental impurities being diminished, the elements with a less than 0.1% mass concentration grew. This explains why the concentration of additional unnamed elements after the cleaning is greater than before cleaning.

Three new elements appeared in the crystal that were not identified prior to the chemical cleaning: Zn, Tm, and Fr. Two possible explanations exist for the presence of these elements. The first is that the 50 nm that was removed was enough material that the x-rays were able to penetrate further into the internal structure of the crystal and reveal the heretofore unseen elements. The second explanation is that deposition occurred from the crown ether/picric acid solution during cleaning. By comparing the new elements that were seen in 041 TU to those found in 003 TU, deposition by the cleaning solution can be ruled out as there is no commonality. Therefore, these elements have to have been present in the crystal prior to cleaning. During the hydrothermal growth, other elements were present in the chamber when taken to high pressures. As the pressure was decreased and condensation began to occur these elements condensed into the crystal along with thorium and uranium producing the total crystal similar to nuclear condensation and fallout processes [5].

Looking at the principal elements in the crystal, a substantial change was witnessed. The thorium concentration saw a small decrease, but nothing particularly noteworthy. Uranium became 50 times more abundant after cleaning than prior to

cleaning despite only appearing in one more point in the grid than prior to cleaning. This is evidence of the amount of surface contamination on the crystal and shows the relatively poor quality of the crystal prior to cleaning, and brings the mass concentration significantly closer to the predicted amount of uranium.

#### ***4.1.2 XRF Results for 041 TU.***

The grid used on 041 TU was chosen to adequately present information on a wide variety of the contours of the crystal as is seen in the upper left corner of Figure 4.1. The surface in this corner is depressed from the otherwise planar face. It is in this depression that the heaviest dopant levels were observed, 24.66% by mass. This is possibly due to fewer surface contaminants being exhibited here due to some manner of fracture occurring at this position enabling the bulk of the crystal material to be more visible. At the other twenty points, a minimum of 20.94% uranium was seen with a mean mass percentage of 22.71%. Nine elements are present in statistically significant amounts besides the two expected.

After cleaning the results are encouraging. The most prevalent elements in the pre-clean sample are yttrium, nickel and cesium. Their mass concentrations were severely diminished after cleaning occurred. Nickel concentration was decreased to 12% of its value before cleaning. Yttrium, cesium, and five other elements are completely removed. The mass concentration of both thorium and uranium increased as a result of the cleaning, by 0.5% and 0.1% respectively.

Similar to the lightly-doped sample, new elements were present in the XRF scan that were not initially seen in the crystal: Cr, Yb, Ga, and Zr. As with 003 TU, because the same methods were used for cleaning both crystals, these elements were probably present in the material prior to cleaning but were not seen by the XRF. The 75 nm that was removed was enough material so that the x-rays were able to penetrate further into the internal structure of the crystal and reveal the heretofore unseen elements. Once again the



prevalence of these elements is probably due to the relatively low initial purity of the growth material.

## 4.2 CASINO Simulations

Table 4.2: CASINO Average Penetration Depths

Sample	Beam Energy (keV)	Average Penetration Depth (nm)
001 TO	3	51
	5	95
	7	150
	10	320
003 TU	3	50
	5	70
	7	100
	10	270
041 TU	3	38
	5	65
	7	85
	10	200
UO <sub>2</sub>	3	48
	5	92
	7	148
	10	250

CASINO simulations of each of the samples was performed in order to determine penetration depths and average dispersion of the electrons for a range of different beam

energies. Figure 4.3 shows the penetration depth of 3 keV electrons and clearly shows that the average penetration depth is in the surface region. Using >3 keV beam energies enables a view of the surface, with 3 keV giving a view of the transition region between the surface and the bulk. The penetration depths show an unexpected trend that as the

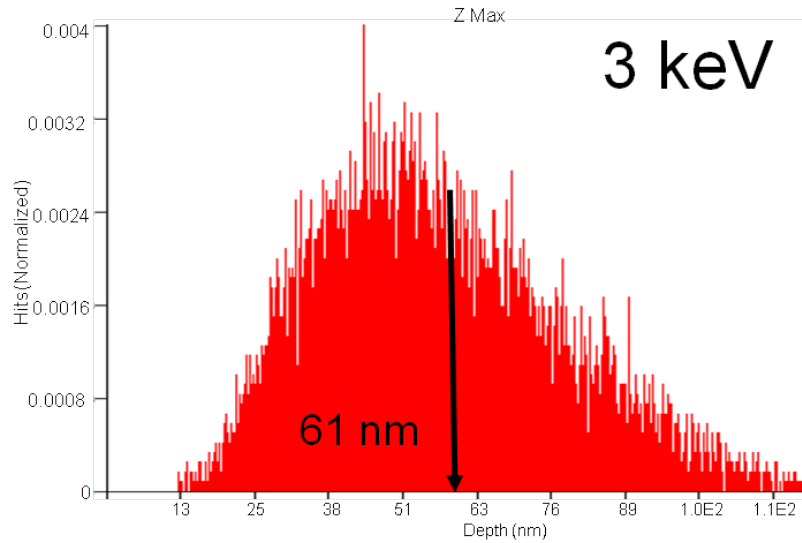


Figure 4.3: CASINO simulation that shows distribution of electron penetration depths into 003 TU using a 3 keV beam energy. The simulation was run using 20,000 electrons and a beam width of 10 nm. 61 nm is the mean penetration depth.

dopant level increases, the average penetration depth decreases; however, penetration depths in pure  $\text{UO}_2$  are greater than those in the alloy. As a result of becoming an alloy, the disruption to the periodic nature of the lattice results in substantial lattice strain that reduces the ability for electrons to travel through it. Once the material loses its alloyed nature by becoming pure  $\text{UO}_2$ , the smaller ionic radii results in a greater density and the close-packed structure of the crystal is more tightly bound. These simulations show that while the electrons experience angular divergence through the crystal, even at high energies, the divergence is not large enough for it to cause any significant loss of signal.

The maximum penetration depth for the highest energy used (14 keV) was  $1.15 \times 10^4 \text{ \AA}$ , which is several orders of magnitude less than the crystal size, ensuring that no electrons passed through the sample to the mounting plate.

### 4.3 Undoped ThO<sub>2</sub> Post-Cleaning

In order to establish baseline measurements and track the changes that occurred to the thorium dioxide structure as increasing levels of uranium are added, it was first necessary to collect spectra for undoped thoria, 001 TO. The side of the crystal used for CL was roughly planar, with few abnormal ridges. DRCL was performed at 3, 5, 7 and 10 keV beam energies using the electron gun with the barium oxide cathode at a source current of 2.4 amps and electron beam fluence between 3 and  $15 \mu\text{A}$ . The results, seen in Figure 4.4, demonstrate a single principal peak whose wavelength of maximum emission occurred at two different positions. The principal peaks' rise corresponds to  $4.98 \pm 0.04 \text{ eV}$  and the peak is not a perfect Gaussian. This is due to it being the combination of several transitions as well as peak broadening due to inhomogeneities in the material.

The change in maximum emission wavelength that occurred is especially noticeable when the spectra are normalized as in Figure 4.5. The two sets of wavelengths can be grouped into two regimes, an  $\alpha$  regime that groups higher energy peaks, and a  $\beta$  regime that groups the lower energy peaks. When interrogated using a lower energy beam, the spectrum has its wavelength of maximum emission at  $3163 \pm 15 \text{ \AA}$  ( $\alpha$ ) and with a higher energy beam at  $3349 \pm 35 \text{ \AA}$  ( $\beta$ ). The difference between these two maxima is  $0.218 \pm 0.039 \text{ eV}$ .

The cause of these two distinct peaks with no intermediary peak emission wavelengths can possibly be explained by one of four different mechanisms. First, because the material is being probed at higher energies, this could be a depth-resolved phenomenon. CASINO simulations show that 5 keV corresponds to an average electron

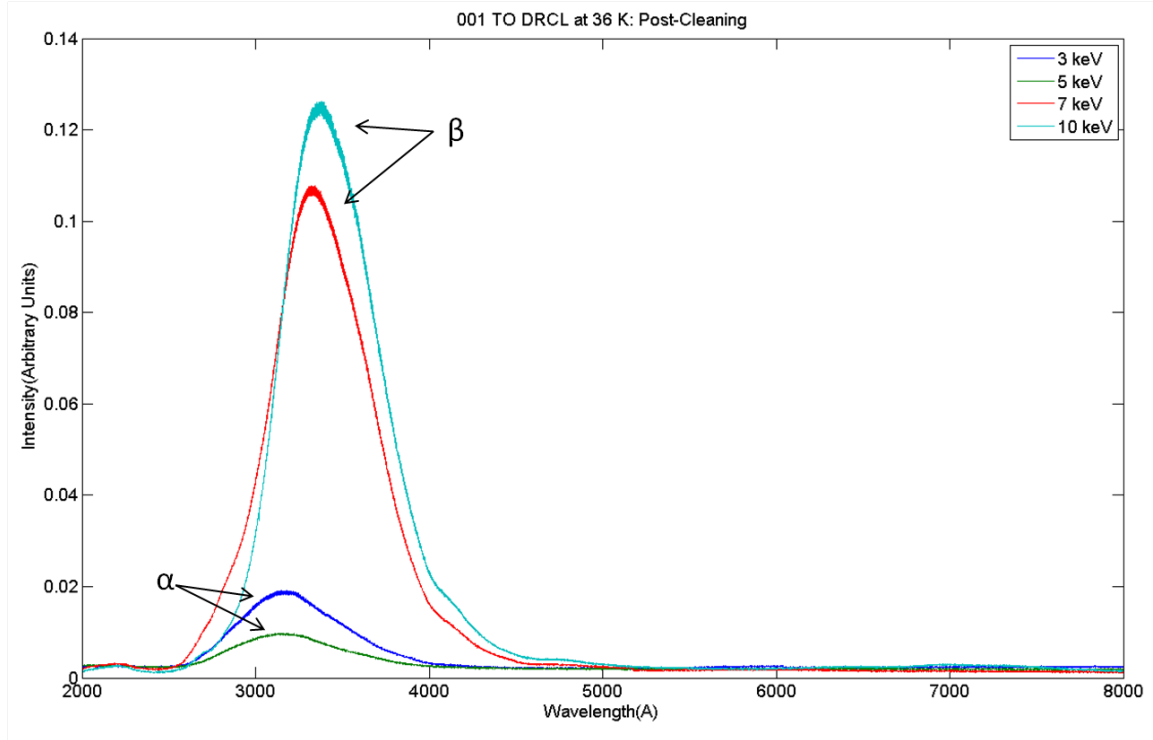


Figure 4.4: DRCL measurements taken for 001 TO post-cleaning in the range of 3-10 keV beam energies. All measurements were conducted at 36 K.

penetration depth of 95 nm, which is well into the bulk even prior to cleaning, so it is likely not a surface artifact especially as this shift was only seen in samples after cleaning. This makes this explanation seem unlikely, especially considering it is also seen later for 003 TU. Secondly, this could be due to charging of the crystal. To investigate this, a series of scans were performed one after another at the same energy, 7 keV, to see if the peak emission wavelength experienced a progressive redshift from the  $\alpha$  transition to the  $\beta$ . Over the course of these scans, no drifting was seen. The peak exhibits a binary nature of either existing at the  $\alpha$  position or at the  $\beta$  position. The third possibility is that due to population filling, i.e. as a result of the heating of the crystal, different transitions are being seen. To investigate this, deconvolutions were performed on each of the two peaks to investigate if the cause of this is a transition between degenerate states, for example O

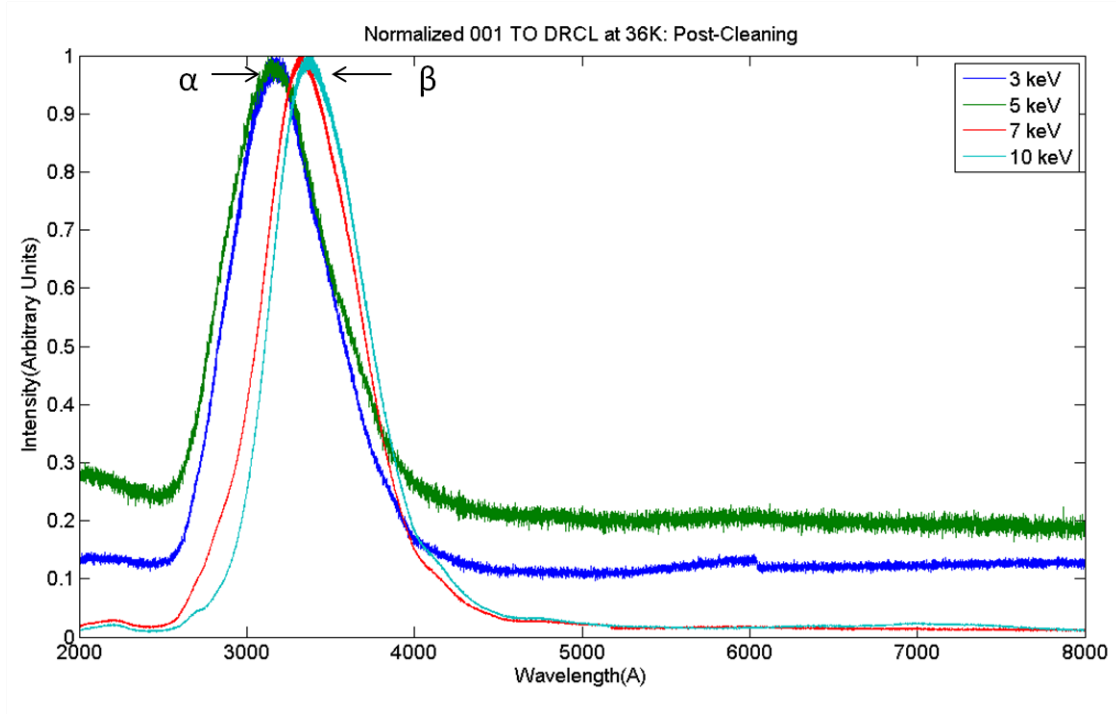


Figure 4.5: Normalized DRCL measurements taken for 001 TO post-cleaning in the range of 3-10 keV beam energies. All measurements were conducted at 36 K.

2p to Th  $6d_{1/2}$  and O 2p to Th  $6d_{3/2}$ . Finally, the suddenness of the shift from the  $\alpha$  to the  $\beta$  position could be a result of a phase transition that is occurring inside of thorium. This would explain the binary nature of the peaks either being at  $\alpha$  or  $\beta$  but never in between. Unfortunately, due to the interest of the scientific community in the high temperature properties of thorium, the phase diagrams that are published deal only with temperatures above 1000 K [3, 8]. The phase diagrams in the literature show no fine detail below 500 K for either uranium dioxide or thorium dioxide.

Upon initial inspection, it appears as if the broad peak shows evidence of multiple smaller peaks convolved into its structure due to slope changes. To investigate this a deconvolution was performed using Gaussian peaks. The software used for this is called Peak Fit. One spectrum with a peak emission wavelength at  $\alpha$  and  $\beta$  were

examined. In order to determine the quality of the fit, the coefficient of determination  $R^2$  was used, which details the strength of a curve fit with a value that ranges from 0-1 with Peak Fit defining 1 to be a perfect fit.

For a spectrum that peaked at point  $\alpha$ , the principal peak was found to be the result of two Gaussian peaks with maxima at 3066.3 and 3485.2 Å and had an  $R^2$  value of 0.998. The strength of the two curve fit to the data suggests that more Gaussian curves are not needed. The transition energy of the 3066.3 Å peak is 4.94 eV. This energy is greater than what is predicted by P. Kelly for the O 2p to Th 6d transition by 0.2 eV (4.8 eV), but could be due to the band splitting that is seen in an under review paper [19]. The second  $\alpha$  peak has its transition energy at 4.21 eV, corresponding to the indirect band gap transition that occurs across the Brillouin zone in the singly degenerate state which is 4.3 eV.

For  $\beta$ , an  $R^2$  value of 0.997 is obtained once again using 2 peaks for the 10 keV spectrum. These two peaks have wavelengths of maximum emission at 3381.9 and 3843 Å respectively. The first peak has its rise at 4.79 eV. This transition corresponds to the direct band gap transition detailed by P. Kelly as a O 2p to Th 6d transition that occurs in the X point at the edge of the Brillouin zone [18, 19]. The second peak sees its rise at 3.65 eV. The transition accompanying the second peak is less clear. Martin states that the anion Frenkel energy is 3.31 eV, which temperature dependent CL has shown to indicate the presence of defects in the crystal [26]. If these defects have Frenkel character then it is possible that this transition is a broadened line shape resulting from these defects. The reason for this shift becomes clearer as comparisons are made between samples and will be further explored in the next section.

TDCL was also performed on this sample, and the results are seen in Figure 4.6. Steps were taken in 40 degree increments, from 37-277 K to view how the sample responded as it was heated. 7 keV was chosen as the beam energy for all measurements as

CASINO simulations showed that at this energy electrons would penetrate into the bulk for all three crystal samples.

The transition energy was found to be  $4.69 \pm 0.1$  eV, and had a wavelength of maximum emission of  $3347 \pm 14.6$  Å which matched that of the  $\beta$  peak seen in the DRCL

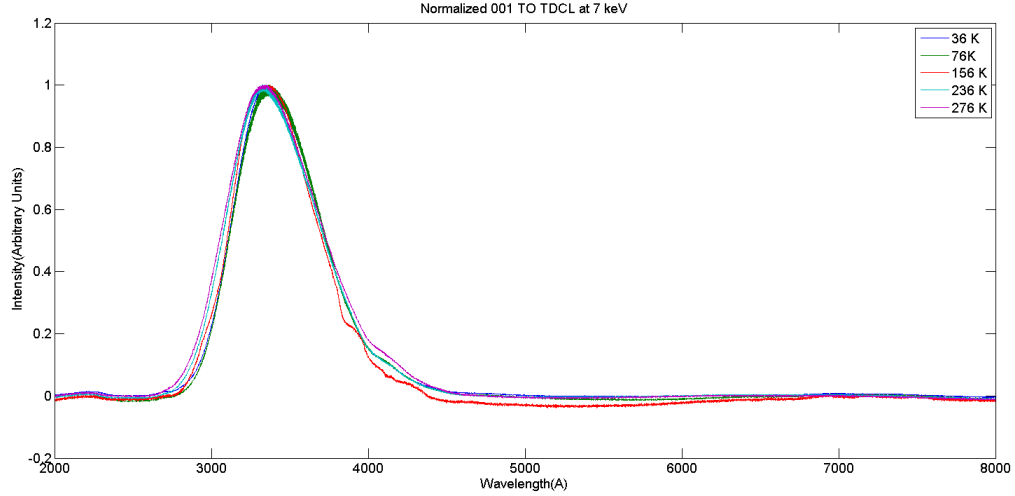


Figure 4.6: TDCL measurements taken for 001 TO from 36-276 K with a constant beam energy of 7 keV.

measurements. Unfortunately, quality spectra were not able to be obtained in the intervals at 76 K and 156 K. There was no discernible change to the spectra as the temperature was increased save for a diminishing intensity which is expected due to the increased phonon presence in the sample. This peak did not display the shift in maximum wavelength that occurred in the DRCL as temperature increased, due to the fact that the peak had already shifted. Once the peak emission wavelength moved from  $\alpha$  to  $\beta$  in all experiments, it did not return to its previous state, with the sole exception being in the hysteresis measurement performed on sample 003 TU. This will be further discussed in the next section.

In summary, the undoped thoria sample showed evidence of peaks in two regimes: 3163 Å ( $\alpha$ ) and 3349 Å ( $\beta$ ). These peaks existed in a binary nature with no intermediate states in between. TDCL showed that as the sample was heated occurred on the sample the peak remained in the  $\beta$  position. Deconvolution showed that each peak was made up of two smaller peaks whose transition energies corresponded to the direct and indirect band gap transitions seen in literature. All deconvolution data is compiled in Appendix B.

#### 4.4 Cathodoluminescence of Lightly-Doped U:ThO<sub>2</sub>

##### 4.4.1 Pre-Cleaning.

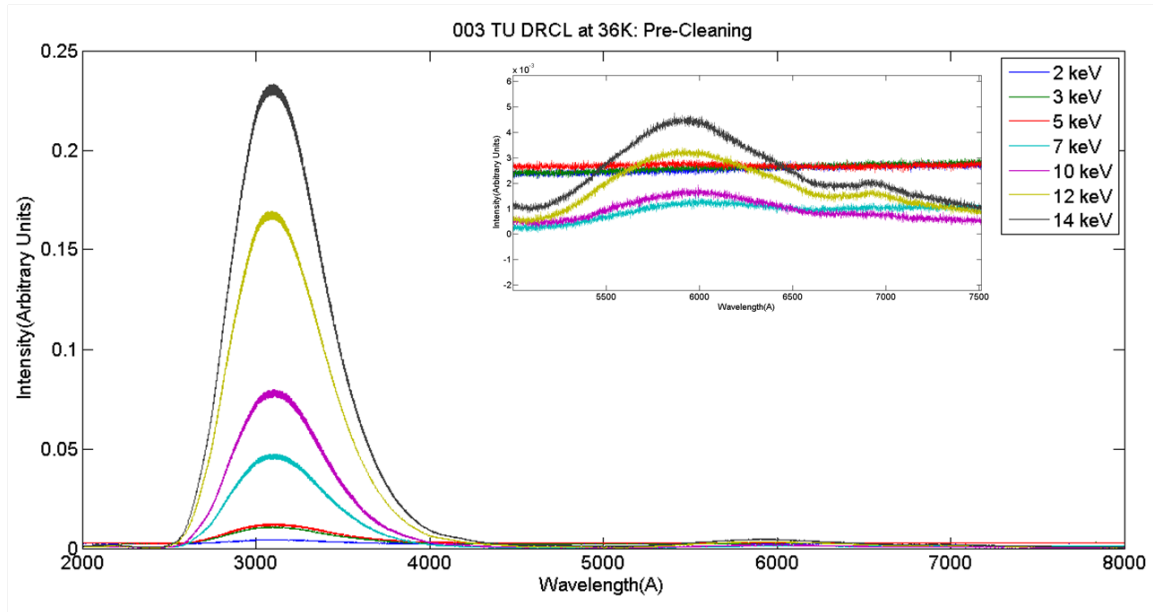


Figure 4.7: DRCL measurements taken for 003 TU pre-cleaning in the range of 2-14 keV beam energies. Insert shows secondary peak in the range of 5300-7500 Å. All measurements were conducted at 36 K.



DRCL and TDCL were conducted on sample 003 TU prior to the chemical cleaning. The sample was .0027 g in mass and is shown in Figure 1.2. Measurements prior to cleaning were performed with the original electron gun operating at a filament source current of 2.2 amps. Pre-cleaning DRCL spectra are shown in Figure 4.7. Upon initial inspection it appears that little has changed between the undoped thoria to the 003 TU sample. The main peak, rising at  $2472 \text{ \AA}$ , corresponds to  $4.91 \pm 0.8 \text{ eV}$  and remains the most distinctive feature of the spectrum. However, upon closer examination many differences arise. The principle peak's maximum emission occurs at  $3090 \pm 6.0 \text{ \AA}$ , a  $73 \text{ \AA}$  blueshift from undoped thoria. Using Peak Fit deconvolution on this peak gives an  $R^2$  of 0.998 using two Gaussian peaks, one whose peak is at  $3076.5 \text{ \AA}$  and a second whose peak is at  $3478.7 \text{ \AA}$ . A compilation of this deconvolution data is provided in Appendix B. Despite the blueshift in the maximum emission wavelength of the spectral peak, the deconvolved peaks have virtually the same wavelengths of maximum emission as the thoria. The transition energies though are blueshifted to 5.07 and 4.26 eV respectively. As seen in literature, the band gap transitions of O 2p to U 6d are 0.2 eV higher than what is reported for O 2p to Th 6d, and the blue shift seen here is indicative of this. However, the poor overall quality of the crystals could also be responsible for this shift. Higher quality crystals would need to be examined in order for a definitive statement to be made.

The insert in Figure 4.7 shows the most noticeable new feature of the crystal, a small, broad peak at  $5934 \pm 44 \text{ \AA}$ . This peak is visible beginning at 7 keV and grows as the beam penetration gets larger. At 14 keV, the peak is 0.02% of the intensity of the principle peak, which curiously enough is the dopant level of the crystal seen using XRF. This peak is broad, with a FWHM of  $996 \text{ \AA}$  and has a transition energy of 2.42 eV. The fact that this peak exists solely in the uranium doped sample is indicative that it is not a system defect. Therefore, this peak is possibly associated with the electric quadrupole transition of O 2p to U 5f. Its weakness in intensity relative to the dipole transitions

present in the main peak is ascribed to its quadrupole nature, which has been shown in T-Matrix simulations of quadrupole transitions [27]. TDCL was performed on the sample with spectra displayed in Figure 4.8. It was expected that different transitions would be witnessed as the increase in temperature resulted in population filling. This may be what occurred, since over the course of the temperature rise, two different transition energies are seen. At 36 K, the 7 keV spectra from the DRCL was used which has a transition energy

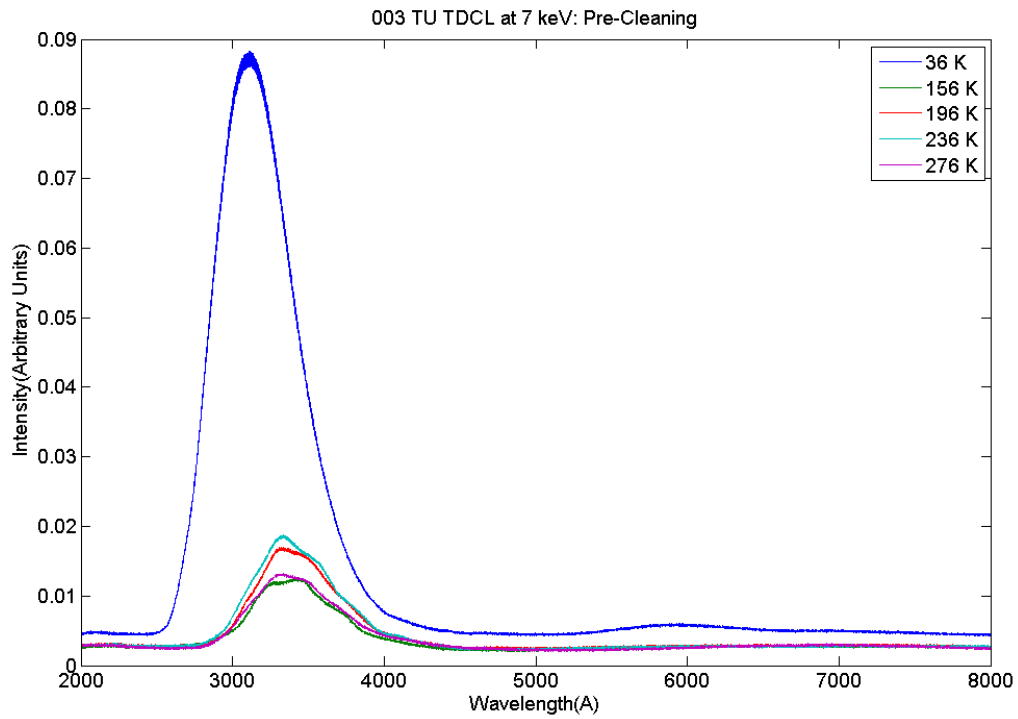


Figure 4.8: TDCL measurements taken for 003 TU from 36-276 K pre-cleaning with a constant beam energy of 7 keV.

of  $4.91 \pm 0.8$  eV. At 156 K and above, all the way to room temperature, the transition energy is 4.45 eV. All of these higher temperature spectra clearly show evidence of two peaks: one at  $3316 \pm 30.6$  Å and the other at  $3444 \pm 16.9$  Å. When run through a two Gaussian Peak Fit, a  $0.997 R^2$  fit is achieved with peaks whose transition energies are 4.60

eV and 3.96 eV, and whose peak centers occur at 3336.5 Å and 3738.1 Å respectively. The 4.60 eV peak lines up precisely with the O 2p to U 6d direct gap transition at the center of the Brillouin zone seen by P. Kelly [18]. The peak at 3.96 eV is unlike any of the peaks seen thus far. It is too high in energy to be a Frenkel-type defect, but too low in energy to be the indirect O 2p-Th 6d transition. Fortunately, post-cleaning spectra show this peak to no longer be present in the material, so its identification is attributed to some kind of surface defect. The TDCL spectra show further evidence of a phase transition occurring as each individual spectrum belongs to one of the two regimes, with no in between states. This could be evidence of a phase transition occurring in the thoria. This may explain the disappearance of the O 2p to U 5f transition at higher temperatures. Secondly, this could be due to the lack of cleanliness on the surface, a topic to be revisited in the next section.

#### ***4.4.2 Post-Cleaning.***

After cleaning, the crystal, upon visual inspection as seen in Figure 1.3, has lost some of the blackness in its hue and is visibly lighter in color. The fact that the surface still retains some of its blackness is due to the tendency of metal oxides to change color in the presence of even as little as a few hundredths of a mole percent of oxygen molecules in excess of what is stoichiometrically required [13]. The mass removed by the cleaning solution was .0005 g.

A repeat of all measurements performed prior to cleaning was conducted after cleaning with exceptional results. The crystal was noticeably brighter under the electron beam. The spectra displayed remarkable variation as seen in Figure 4.9. Prior to cleaning, at all energies, the data lined up at  $3090 \pm 6$  Å with a single principle peak. After cleaning, there are clearly two separate wavelengths that the data moves between, one at  $3059 \pm 13$  Å ( $\alpha$ ) and aligns with the 10 keV spectrum in Figure 4.9. The other wavelength is at  $3250 \pm 12$  Å ( $\beta$ ) and aligns with the 14 keV spectrum in Figure 4.9, similar to what occurred in undoped thoria.

As in undoped thoria, there is no evidence that charging is occurring. The spectra very clearly are divided into either the  $\alpha$  or  $\beta$  regions. The transition energy remains constant at  $5.10 \pm 0.06$  eV regardless of the wavelength at which the peak intensity occurs, which indicates that these two transitions occur almost at the same energy in the band structure. The Th 6d band is split into two separate regions in accordance with the degeneracy in DOS calculations which could account for this. Alternatively, the higher energy peaks were taken later than the lower energy peaks. As a result of the interaction of the electron beam with the surface of the sample, heating could be occurring on the surface. The temperature controller only gives information about the temperature on the back surface of the sample touching the cold finger. Therefore, there could be a phase

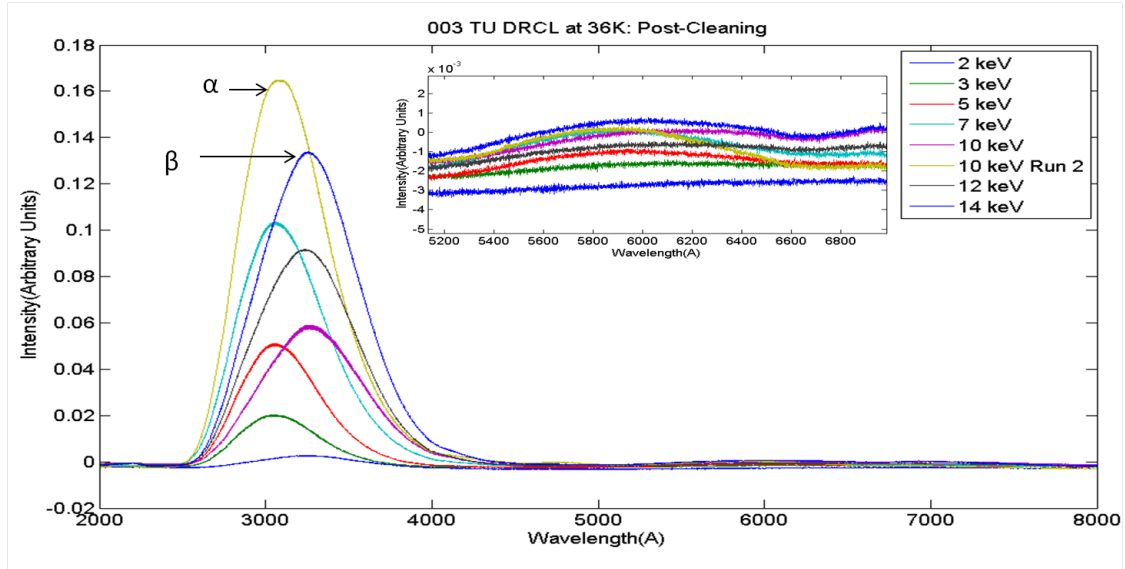


Figure 4.9: DRCL measurements taken for 003 TU post-cleaning in the range of 2-14 keV beam energies.  $\alpha$  peaks are all those whose maximum is at  $3059 \pm 13$  Å, and  $\beta$  peaks are all those whose maximum is at  $3250 \pm 12$  Å. Insert shows secondary peak in the range of 5300-7500 Å. All measurements were conducted at 36 K.

transition occurring due to the electron beam heating the sample to a considerably higher temperature than the controller indicates.

Using Peak Fit, an  $\alpha$  and  $\beta$  peak were deconvolved. The 10 keV  $\alpha$  spectrum was able to be resolved with an  $R^2$  value of .998 using two Gaussian peaks: one peak at 3060.8 and the other at 3472 Å. The 3060 Å peak corresponds to a transition energy of 5.05 eV. Despite this peak corresponding exactly to the O 2p to U 6d transition energy of 5 eV, the small amounts of inconsistently placed uranium in the sample makes it difficult to ascertain whether this is the O 2p to U 6d transition or just a broadened O 2p to Th 6d transition [23]. The 3472 Å peak has a transition energy of 4.26 eV, which is situated on the indirect O 2p to Th 6d transition. The second peak is the 14 keV peak at  $\beta$  and was resolved into two Gaussian peaks with peak emission wavelengths of 3222.5 and 3618.1 Å. The first peak is fairly broad and gave a transition energy of 5.02 eV, which is the same as that of the first  $\alpha$  peak despite the fact that the peak occurred at 3060 Å. This leads to the conclusion that this peak again is associated with the O 2p to Th 6d transition. Similarly, the second peak has its transition energy at 4.06 eV, slightly less than its equivalent  $\alpha$  peak despite once again being red shifted by 200 Å. These results seem to indicate that the same two transitions are occurring in both sets of spectra, but the peak emission wavelength is shifting. To investigate if this was a depth-resolved phenomena, spectra were taken after the shift had occurred to the  $\beta$  region at lower energies. Once the shift in peak wavelength occurred, it was not seen to shift back regardless of the beam energy used.

Analogous to the DRCL spectra, the TDCL spectra can be grouped into two general peak emission regions; however, the location of these two peaks is not the same as is seen at different beam energies using DRCL. The higher energy peak occurs at  $3050 \pm 39.8$  Å, which is in line with the high energy ( $\alpha$ ) peak in 003 TU DRCL. The lower energy peak is located at  $3351 \pm 5.0$  Å. Rather than conforming to the  $\beta$  peak in 003 TU, this

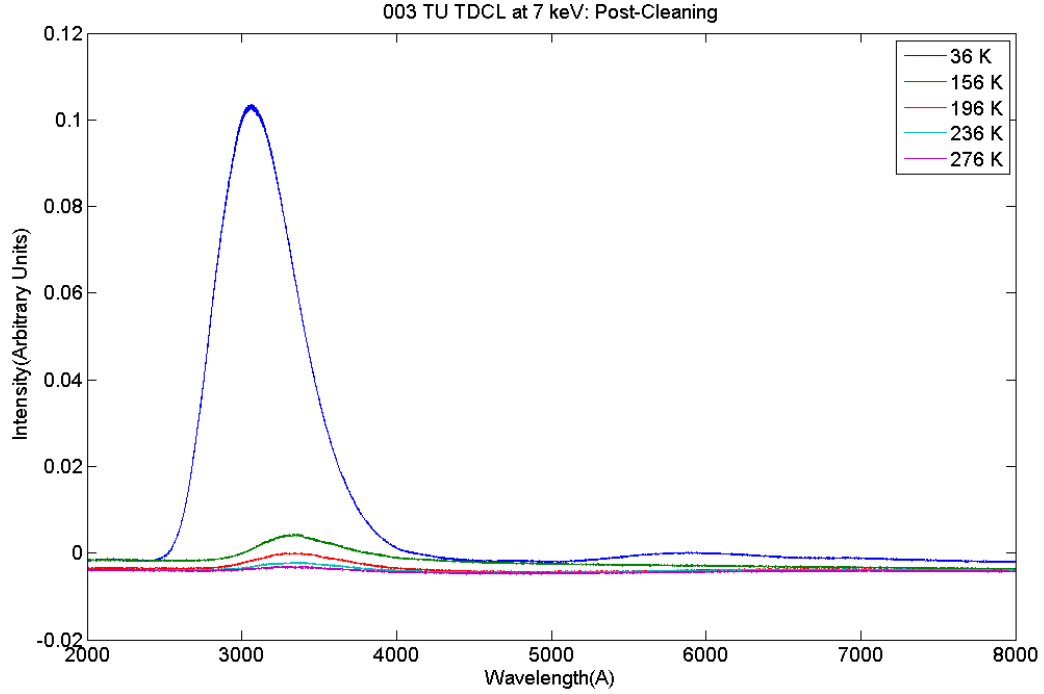


Figure 4.10: TDCL measurements taken for 003 TU from 36-276 K post-cleaning with a constant beam energy of 7 keV.

peak falls on top of the  $\beta$  peak in 001 TO. The transition energy for this peak is  $4.41 \pm .11$  eV, which has been attributed to the indirect O 2p to Th 6d transition. This peak is similar to the deconvolved 001 TO  $\beta$  peak though at slightly lower energies. The spectra of the peak at  $\beta$  are those at higher temperatures (above 156 K). The possibility then arises that the transfer from one peak to the other is related to the heating of the lattice; however, the thermal expansion coefficients of both thorium and uranium dioxide are so low, that a change of a hundred degrees causing a substantial expansion in the material is unlikely. It is more likely that because each band is not perfect, but rather tails off, what is occurring is that populations in the band are filling and that the energy of the transition is shifting to the bottom of the band tail. This is why after 156 K, there is no further shift seen. This could explain the DRCL spectra, as only those spectra that were taken after long periods

of exposure to the electron beam experienced the shift. This does not explain why the transition occurs suddenly with no sign of any intermediate states. The presence of the shift in TDCL indicates that a phase transition may be occurring somewhere between 36 K and 156 K. This temperature regime in the literature is entirely vacant. Each scan takes approximately 2 hours to perform and with four spectra being taken prior to the shift occurring, a significant amount of exposure time takes place. The transition energy once again red shifted with increasing temperature to the same value as was seen before cleaning.

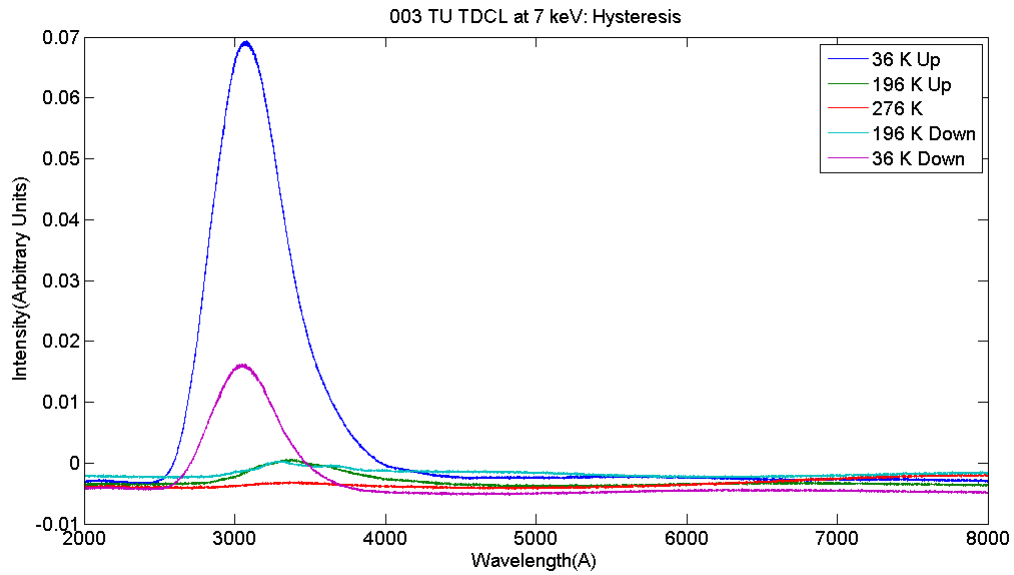


Figure 4.11: Hysteresis TDCL measurements taken for 003 TU from 36-276 K with a constant beam energy of 7 keV.

A thermal hysteresis measurement was conducted to confirm the presence of defects in the crystal. Several papers have demonstrated that anion Frenkel defects are common in both urania and thoria with thoria having a Frenkel energy of 3.31 eV [26]. Intensity aside in the case of 36 K spectra, the spectra as the temperature rises to 276 K is

shadowed by the spectra as the temperature falls from 276 K with little variation. The 36 K spectra peak at  $3060 \pm 15.6 \text{ \AA}$  with a transition energy of  $5.05 \pm 0.02 \text{ eV}$ . The two 196 K peaks exhibit evidence of two peaks at  $3320 \text{ \AA}$  and  $3621 \text{ \AA}$  and transition energies of  $4.39 \pm 0.02 \text{ eV}$ . This symmetry provides evidence for defects, though the defect type can not be determined just from this study.

In summary, before chemical cleaning all DRCL measurements showed evidence of a single peak at  $3090 \pm 6.0 \text{ \AA}$  slightly blue shifted from the undoped thoria, which shows that the introduction of uranium into the crystal is having some effect on the electronic structure of the material. Post-cleaning DRCL spectra exhibited the same binary peak structure as was seen in 001 TO, with the peak emission wavelength occurring at either  $3059 \pm 13 \text{ \AA}$  ( $\alpha$ ) or  $3250 \pm 12 \text{ \AA}$  ( $\beta$ ). A deconvolution of a peak at each of these positions showed evidence of direct and indirect band gap transitions to the Th 6d or U 6d bands in the material. All deconvolution data is compiled in Appendix B. Furthermore, a small peak was seen at  $5934 \pm 44 \text{ \AA}$ . that could be evidence of the O 2p to U 5f band gap transition. TDCL showed collaborating evidence for a phase transition occurring in the material as well as the presence of defects in the material, with anion Frenkel defects being the likely candidate.

## **4.5 Cathodoluminescence Heavily-Doped U:ThO<sub>2</sub>**

### ***4.5.1 Pre-Cleaning.***

Sample 041 TU is a cubic crystal .5 cm x .3 cm x .3 cm. in size, black in color and containing 22% uranium mass concentration. When compared to the undoped and lightly doped thoria samples, the intensity of the CL from this heavily doped crystal was significantly diminished under the same conditions. This is probably as a result of the decrease of OH<sup>-</sup> ions caused by the acidity decreasing due to uranium ions having complete selectivity for formic acid dehydration caused by uranium oxide catalyzation



[4]. The net result is that lattice defects caused by oxygen ions are now removed from the crystal [4].

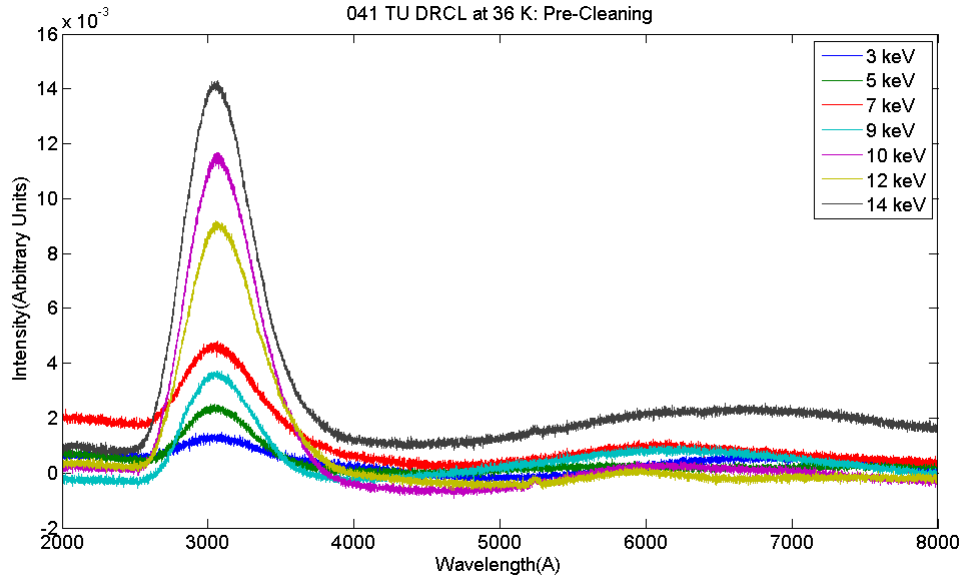


Figure 4.12: DRCL measurements taken for 041 TU pre-cleaning in the range of 2-14 keV beam energies. All measurements were conducted at 36 K.

Looking at the spectra, independent of the diminished signal-to-noise ratio, the spectra at all energies have a principle peak at  $3048 \pm 12 \text{ Å}$  with no variation regardless of where on the crystal the beam is positioned. The transition energy of this peak is found to be  $4.88 \pm 0.12 \text{ eV}$ , which is equivalent to that of the pre-cleaning 003 TU DRCL spectra. The broad peak that is seen in the spectra of the lightly-doped crystal that peaked at  $5964 \text{ Å}$  in the cleaned sample was not seen nearly as separated from the noise as it was in the low doped sample; however, when the spectra are normalized relative to the principle peak, the intensity of the peak is seen to have increased substantially relative to the main peak. The peak is most prominent in the 9 keV spectrum in the normalized data. In this graph, the intensity of the peak at  $6131 \text{ Å}$  has a relative intensity of 0.263, as compared to

the peak in an equivalent spectrum in 003 TU, (10 keV) in Figure 4.9, which has an intensity of 0.002. The peak has increased in relative intensity by 114x to almost a quarter of the relative intensity of the peaks overall. Further, it seems that there is an almost linear relationship between the relative intensity of the peak in comparison to the uranium concentration seen in the material. This would seem to indicate that  $\text{UO}_2$  is being formed; however, the peak is inconsistent at best.

The second unique feature of these spectra is a small peak at  $5239 \pm 3.32 \text{ \AA}$ . This feature is only visible when using beam energies greater than 10 keV. The lack of broadening in the peak ( $\text{FWHM} = 47 \pm 4 \text{ \AA}$ ) as well as its almost negligent intensity relative to the noise floor indicates that this is due to an impurity in the material. Curiously though, the transition energy for this small peak is at 2 eV, right at the start of the upturn of the broad peak, which is also the band gap of  $\text{UO}_2$  [36].

Due to the extremely low signal from the sample at 36 K, it is not surprising that as temperature rose, the S/N ratio diminished accordingly. Spectra taken at 76 K had such low S/N that all spectrum taken, even up to 14 keV beam energy, resulted in a peak maximum that was nearly undistinguishable from the noise floor. As such, prior to the cleaning, no temperature dependent measurements were able to be performed.

#### ***4.5.2 Post-Cleaning.***

Due to the large volume of 041 TU, the concentration of picric and crown ethers was doubled from that used in the 003 TU solution as detailed in Table 3.1. Furthermore, 041 TU was left in the solution for 22 hours, and was vacuum dessicated at  $180^\circ\text{C}$  for an equal amount of time. In this time the crystal lost 0.0256 g. Through volumetric analysis, this was determined to be approximately  $750 \text{ \AA}$  uniformly removed from the surface, which resulted in a net loss of 7% of the total mass removed achieving a final weight of 0.3382 g. In both the pre- and post-cleaning studies the wavelength of maximum emission remained constant at  $3045 \pm 9.5 \text{ \AA}$ . Keeping with what occurred in the lightly-doped

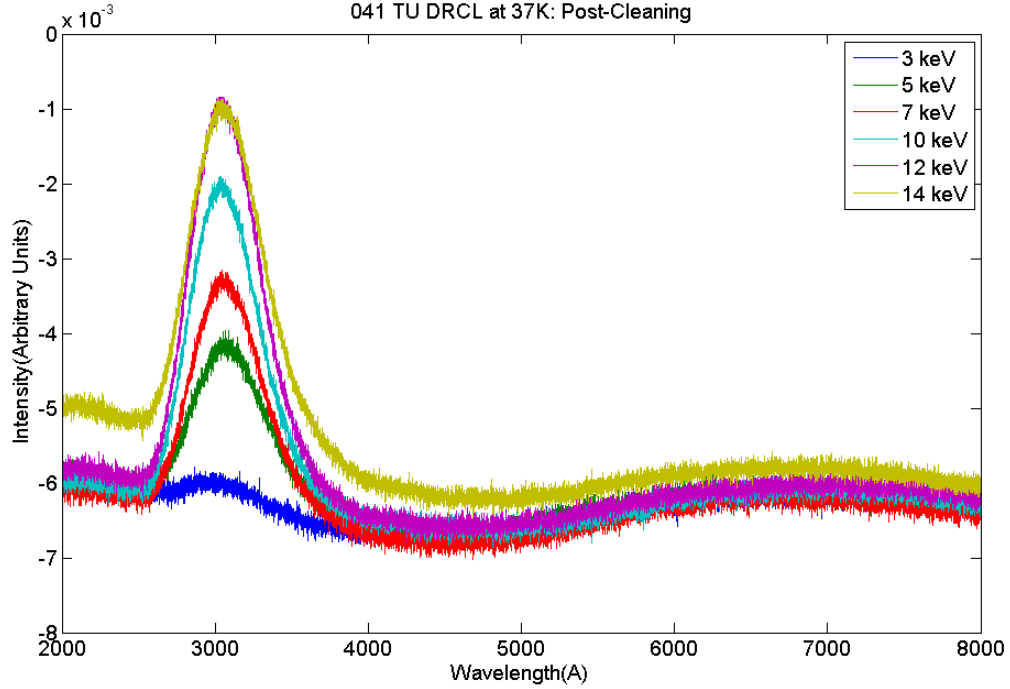


Figure 4.13: DRCL measurements taken for 041 TU post-cleaning in the range of 2-14 keV beam energies. All measurements were conducted at 36 K.

sample, the transition energy increased after cleaning to  $4.98 \pm 0.15$  eV. However, the previous value for the transition energy is within the standard deviation of the pre-cleaning spectra. This seems to indicate no change in the two spectra. When performing a deconvolution of the two 14 keV spectra for the material, one before cleaning and one after, some differences are noted though they are not substantial. Before cleaning, an  $R^2$  value of 0.953 is obtained for a 2 Gaussian deconvolution, and after cleaning the value increased slightly to 0.959. These correlation coefficients are worse than those for the other two samples due to the diminished S/N ratio in the spectra. Before cleaning, the deconvolution shows two peaks with wavelengths of maximum emission at  $3057.4 \text{ \AA}$  and the second at  $3338.2 \text{ \AA}$ . These peaks are blueshifted after cleaning to  $3042.5 \text{ \AA}$  and the  $3367.8 \text{ \AA}$  which is in accordance with the blue shift seen in emission curve. The transition

energies are also blueshifted, from 4.93 and 4.24 eV in the pre-cleaning spectra to 5.18 and 4.35 eV in the post-cleaning spectra. This deconvolution data is compiled with the other samples in Appendix . The higher energy transition is possibly attributed to the direct band-gap transition in  $\text{UO}_2$ , and the lower energy transition to the indirect band gap transition in  $\text{UO}_2$  from the O 2p band to the U 6d band. No evidence of the binary peak shifting seen in the undoped and lightly-doped spectra is visible in 041 TU. As a result, this leads to the possible conclusion that a phase transition is occurring in thoria that is not present in urania. There is a greater homogeneity in the behavior of the spectra past

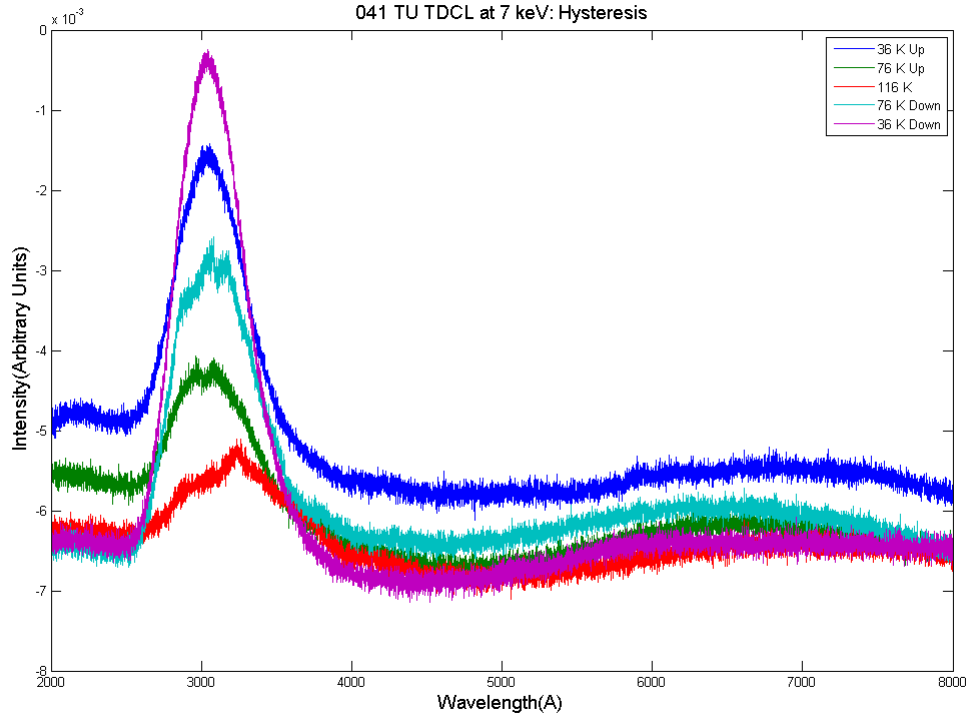


Figure 4.14: Hysteresis TDCL measurements taken for 041 TU from 36-116 K with a constant beam energy of 7 keV.

5000 Å with the intensity of the 5000 Å peak being almost constant regardless of the

beam energy used. This could be indicative of a high amount of uranium content near the surface of the crystal post-cleaning. There is still no evidence of the singular peak at 4700 Å published by Winer [43]. As the concentration of uranium increases to form more  $\text{UO}_2$ , it is possible that this peak will eventually be formed by the convolution of the broad peak at 5000 Å and the main emission peak at 3050 Å. Of note, the small peak at 5240 Å has been removed which indicates that it was due to a surface impurity that was stripped off during cleaning. After cleaning, temperature studies proved to be much more fruitful and despite the small S/N, measurements were able to be performed up to 116 K. This enabled the investigation of defects in the crystal using hysteresis. Similar to what is seen in the lightly-doped crystal, in 041 TU the 36 K spectra are identical in terms of waveform, maximum emission wavelength, and transition energy. There is slight variation in the 76 K spectra, with the peak width being broader and more defined at the center of the plateau, but nothing that can be definitively claimed as different about the spectra. The features at the center of the main emission peak in the 76 K spectra were not able to be reproduced and are ascribed to fluctuations either in the gun or in the environment.

In summary, the S/N ratio was found to be significantly diminished with respect to the lightly-doped and undoped thoria samples. An emission peak at  $3045 \pm 9.5$  Å was observed as well as was a secondary broad peak at  $6131 \pm 244$  Å. The cleaning did not have a sizeable effect on the DRCL spectra, and no evidence of the binary peak shift that occurred in the lightly-doped and undoped samples was observed. A deconvolution of one of the spectra shows evidence of two peaks that correlate to the band gap transition of  $\text{UO}_2$  from the U 6d conduction band to the O 2p valence band. All deconvolution data is compiled in Appendix B. The peak at 6131 Å remains broad and is tentatively ascribed to emission from a transition between the U 5f band to the O 2p band.

## V. Conclusion

A summary of the results and analysis derived from the cathodoluminescence spectra for each sample acquired over the course of this thesis are given here. In addition, a road map for future work is laid out.

### 5.1 Summary of Results

#### 5.1.1 XRF and Chemical Cleaning.

X-ray fluorescence measurements were taken prior to and subsequent to the chemical cleaning using a crown ether/picric acid solution. Weighing the samples and performing volumetric analysis on the samples showed that the amount of surface removal can be controlled so as to strip off the desired amount of material. The XRF spectra gave evidence that large amounts of impurities were removed as a result of this cleaning, indicating its usefulness in removing surface contaminants in actinide oxides. Furthermore, substantial differences were seen in the CL spectra of the lightly-doped thoria (003 TU) sample after cleaning. In the lightly-doped sample, the uranium was inhomogeneously distributed through the sample appearing in only of five of the twenty points that were examined. This non-uniformity means that it is more likely that pockets of  $\text{UO}_2$  were formed rather than uranium substituting for thorium in the fluorite structure. In the heavily-doped sample (041 TU), uranium was observed in all twenty points and was uniformly distributed.

#### 5.1.2 Cathodoluminescence.

Depth resolved cathodoluminescence was used to examine the interband transitions in all three single crystals. In all three crystals the primary feature of the spectra was a large principle peak. In undoped thoria, the transition occurred at either  $3163 \pm 15 \text{ \AA}$  or  $3349 \pm 35 \text{ \AA}$  with both peaks rising at the same energy. When

deconvolved, evidence is seen for both the direct band gap O 2p to Th 6d  $4.76 \pm 0.26$  eV transition at the center of the Brillouin zone and an indirect band gap O 2p to Th 6d  $4.13 \pm 0.11$  eV transition from the center to the edge of the Brillouin zone. There is also possible evidence for anion Frenkel defects with energy of  $3.65 \pm 0.15$  eV.

In lightly-doped thoria, a similar splitting occurs with the two peaks at  $3059 \pm 13$  Å and  $3250 \pm 12$  Å. The blue shift seen in the spectra with respect to those seen in undoped thoria is possibly a result of the transitions shifting from thorium bands to uranium bands. When deconvolved, both peaks were found to be made of two smaller peaks with transition energies of  $4.12 \pm 0.08$  eV and  $5.04 \pm 0.02$  eV. The two deconvolved peaks that form the 3250 Å peak are broadened with respect to those seen in the 3059 Å peak. The 4.12 eV transition corresponds to either the indirect band gap transition of O 2p to Th 6d or O 2p to U 6d. The 5.04 eV transition corresponds to either the direct gap O 2p to Th 6d or O 2p to U 6d. The reason for the shift in peaks is attributed to either population filling as was seen in the temperature dependent studies that were conducted or a phase transition in thoria that does not occur in urania. The phase transition accounts for the binary nature of the shift with no progression in the wavelength of maximum emission seen. Finally, the spectra from the heavily-doped crystal contains a peak at  $3048 \pm 13$  Å similar to that from the lightly-doped sample, but exhibited no shift in wavelength. Its deconvolution showed the same peaks as were seen in the equivalent peak in lightly-doped thoria.

As the dopant level increased, a small broad peak began to grow at  $5934 \pm 44$  Å in lightly doped thoria and  $6131 \pm 244$  Å in heavily-doped thoria. As the dopant level increased, so too does the intensity of the peak. In the lightly-doped thoria sample, the uranium concentration after cleaning was found to be 1%, and the intensity of the peak was 0.05% of the main peak. In the heavily-doped thoria sample the peak had increased in intensity to over 20% indicating a correlation that should be explored in future work. This

peak is possibly associated with to the quadrupole band gap transition of O 2p to U 5f which explains both its broadness and its weakness in intensity in comparison to the main peak and correlates well with the  $\text{UO}_2$  band gap of 2.4 eV seen in literature.

Temperature dependent cathodoluminescence showed evidence of defects in all three of the crystals which provides additional evidence for possibly associating the anion Frenkel defects with the 3.65 eV transition seen in the undoped thoria.

## **5.2 Future Research**

While the crystals studied in this thesis have been extensively characterized using cathodoluminescence, there is still much work to be done. The crystal quality of the uranium doped crystals needs to be investigated using x-ray diffraction, and a rocking curve established. Furthermore, the extreme optical discoloration, small size, and non-planar faces of the crystals posed problems in this thesis. For future work larger crystals or cleaved crystal samples would be ideal. The dopant levels of the crystals used were severely limited. For future projects, it would be beneficial to have access to a wider variety of uranium concentrations in thorium oxide crystals or pure uranium oxide crystals. Growth of all of these is currently being pursued at AFIT and AFRL.

Currently, a photoemission system is being built that would allow for several new measurements to be made. First, the system will be able to provide for argon ion sputtering as well as annealing of samples. This will provide a clean surface which is imperative for emission studies. A low energy electron diffraction system will provide confirmation of the homogeneity of the surface as well as the state of its cleanliness. An x-ray and an ultraviolet light source are being mounted onto the system to perform x-ray photoelectron spectroscopy and ultraviolet photoelectron spectroscopy respectively. These methods will provide information about inner valence molecular orbitals, specifically targeting the Th 4f and O 1s orbitals. This information, in combination with this thesis



work, will form a more complete picture of the electronic structure of  $\text{U}_x\text{:Th}_{1-x}\text{O}_2$  than what was able to be provided in this thesis.

The motivation for this research is to provide a new material for use as a nuclear detector by way of neutron interaction. Therefore, a final piece of future research would be in conducting neutron bombardment experiments to investigate how  $\text{U}_x\text{:Th}_{1-x}\text{O}_2$  reacts. That investigation is far down the road.

## Appendix A: CL System Parts List

Table A.1: Equipment List for CL System

Component	Manufacturer	Model/Serial Number	Specs
1st Electron Gun	Kimball	EMG-12B/220DZ	Beam Energy Range: 1-20 keV
2nd Electron Gun	Kimball	EFG-12B/220DZ	Beam Energy Range: 1-20 keV
Coolpower 4.2 Refrigerator	Leybold	NE-5302	Stage One: T=34 K, Stage Two: T=3 K
Dry Scroll Pump	Varian	50668	Pump Speed: 500 L/min
HiPace 80 Turbo Drag Pump	Pfeiffer	79062008	67 L/s for N <sub>2</sub>
Turbo-molecular pump	Agilent	IT1211	250 L/s for N <sub>2</sub>
Vac-ion Pump	Varian	929-7008/649T	300 L/s for N <sub>2</sub>
Spectrometer	Jobin Yvon–SPEX	500M/6650011420-866RH	$\lambda_{range}=1000-8000 \text{ \AA}$
PMT Housing	Products for Research Inc	19941-95	Operating Temp: 70-300 K
Data Acquisition Software	SynerJY	N/A	Windows OS

## Appendix B: Deconvolution Table

Table B.1: Deconvolution Spectral Comparison Results

Spectrum	Spectral Peak	Transition	$\lambda_{max}(\text{\AA})$	$E_{Transition}(eV)$	$R^2$
Clean 001 TO	$\alpha$	ThO <sub>2</sub> Direct Gap	3066.3	4.94	0.998
		ThO <sub>2</sub> Indirect Gap	3485.2	4.21	0.998
Clean 001 TO	$\beta$	Direct Gap	3381.8	4.79	0.997
		Anion Frenkel Defect	3843.7	3.65	0.997
Dirty 003 TU	$\alpha$	ThO <sub>2</sub> Direct Gap	3076.5	5.07	0.998
		ThO <sub>2</sub> Indirect Gap	3478.7	4.26	0.998
Clean 003 TU	$\alpha$	ThO <sub>2</sub> Direct Gap	3060.8	5.05	0.998
		ThO <sub>2</sub> Indirect Gap	3472.4	4.17	0.998
Clean 003 TU	$\beta$	ThO <sub>2</sub> Direct Gap	3222.5.8	5.02	0.998
		ThO <sub>2</sub> Indirect Gap	3618.1	4.06	0.998
TDCL Dirty 003 TU	$\beta$	ThO <sub>2</sub> Indirect Gap	3286.1	4.27	0.953
		Anion Frenkel Defect	3574.3	3.87	0.953
TDCL Clean 003 TU	$\beta$	ThO <sub>2</sub> Direct Gap	3292.1	4.65	0.973
		Anion Frenkel Defect	3564.1	4.18	0.973
Dirty 041 TU	$\alpha$	UO <sub>2</sub> Direct Gap	3057.4	4.93	0.953
		UO <sub>2</sub> Indirect Gap	3338.2	4.24	0.953
Clean 041 TU	$\alpha$	UO <sub>2</sub> Direct Gap	3042.5	5.18	0.959
		UO <sub>2</sub> Indirect Gap	3367.8	4.35	0.959

## Appendix C: CL Spectral Data

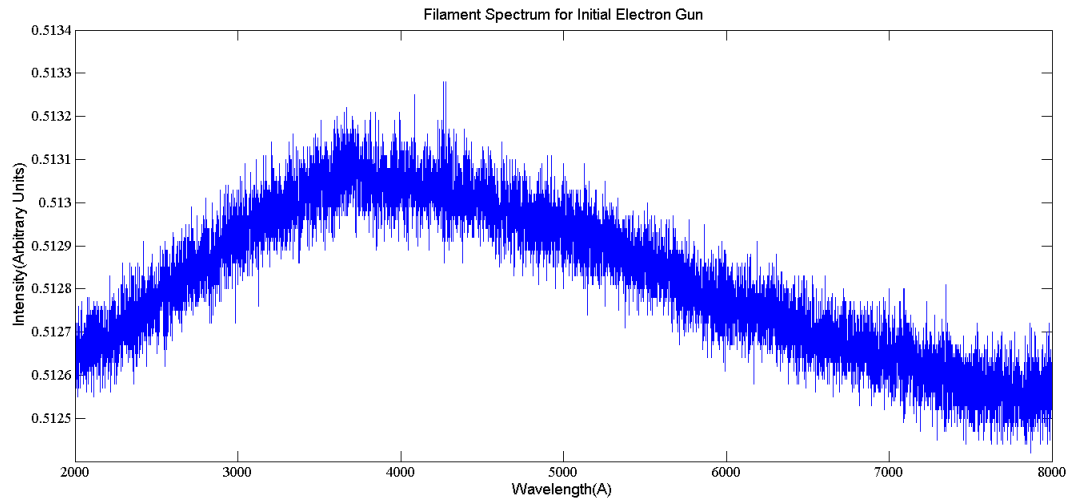


Figure C.1: Thoriated tungsten filament spectrum taken for the first electron gun used. This spectrum was taken using a beam energy of 0 keV and a source current of 2.4 amps consistent with the current used in all measurements taken and was directed onto an empty sample holder. This spectrum was subtracted out from data taken using this gun.

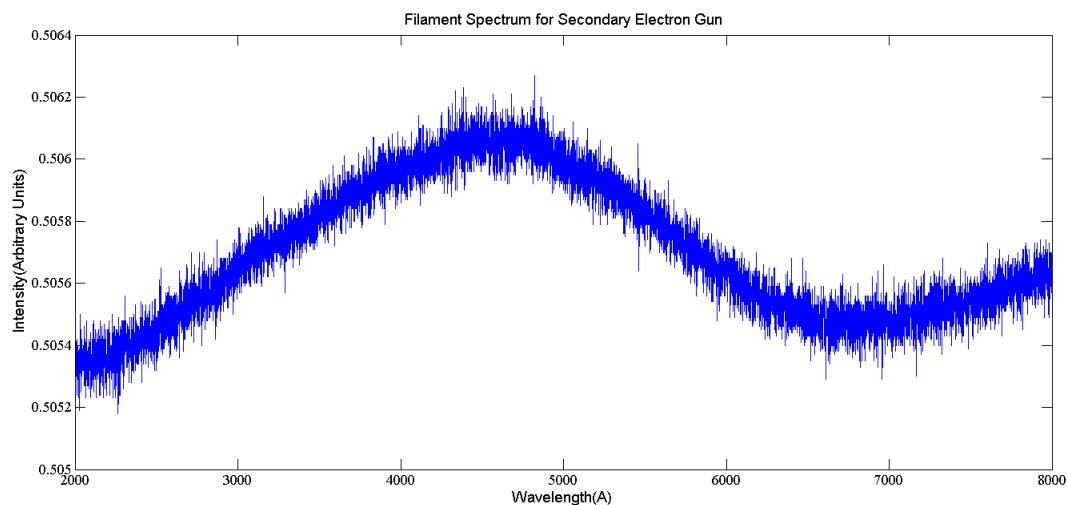


Figure C.2: Barium oxide filament spectrum taken for the second electron gun used. This spectrum was taken using a beam energy of 0 keV and a source current of 1.63 amps consistent with the current used in all measurements taken and directed onto an empty sample holder. This spectrum was subtracted out from data taken using this gun.

## Appendix D: Supplementary Casino Data

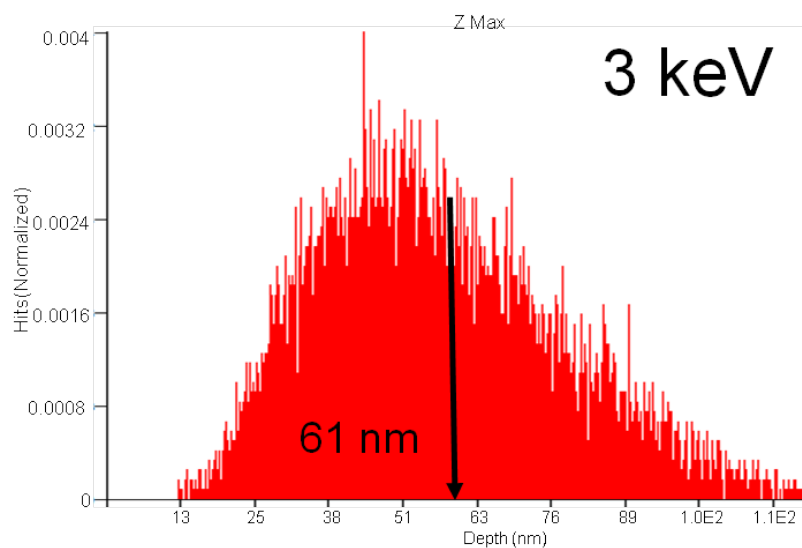


Figure D.1: CASINO simulation that shows distribution of electron penetration depths into 001 TO using a 3 keV beam energy. The simulation was run using 20,000 electrons and a beam width of 3 nm. 61 nm is the mean penetration depth.

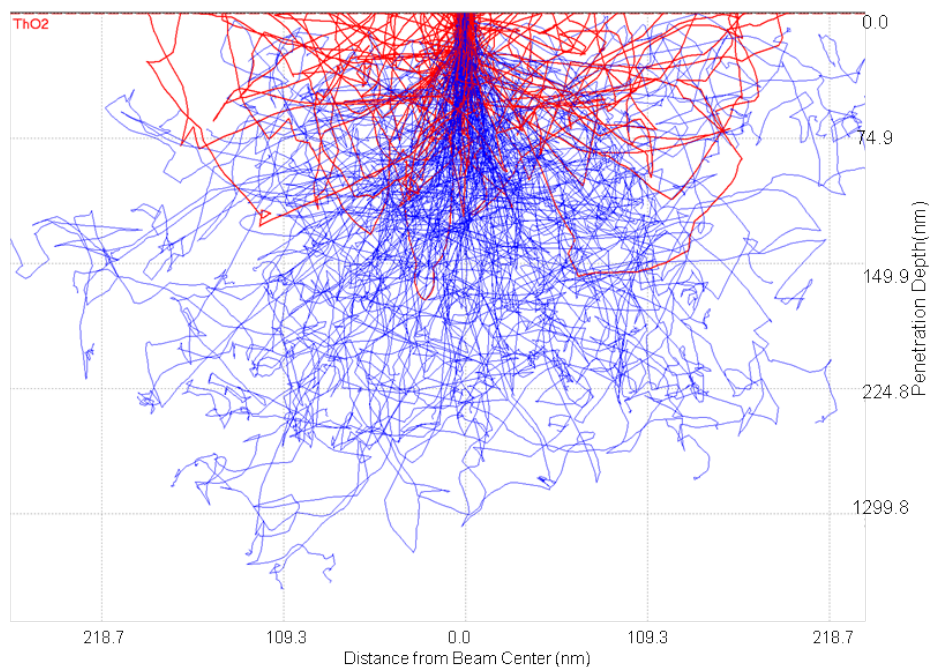


Figure D.2: CASINO simulation for electron pathways into 001 TO with 7 keV beam energy. The simulation was run using 20,000 electrons and a beam width of 10 nm for the effect of this display. Lines in red are back-scattered electrons and blue lines show non-back scattered electrons.

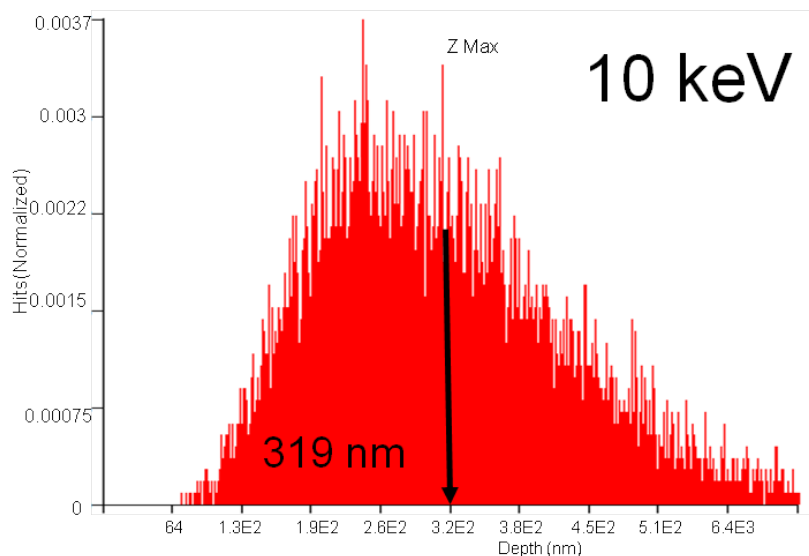


Figure D.3: CASINO simulation that shows distribution of electron penetration depths into 001 TO using a 10 keV beam energy. The simulation was run using 20,000 electrons and a beam width of 10 nm. 319 nm is the mean penetration depth.

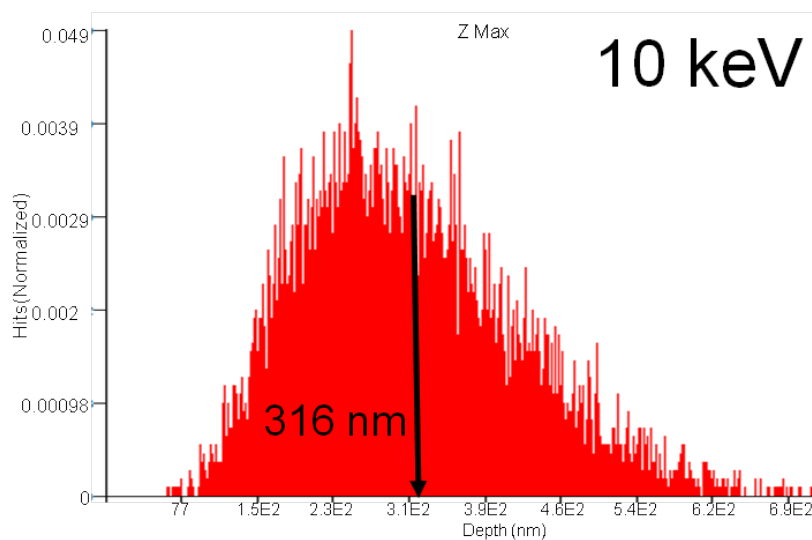


Figure D.4: CASINO simulation that shows distribution of electron penetration depths into 003 TU using a 10 keV beam energy. The simulation was run using 20,000 electrons and a beam width of 10 nm. 270 nm is the mean penetration depth.



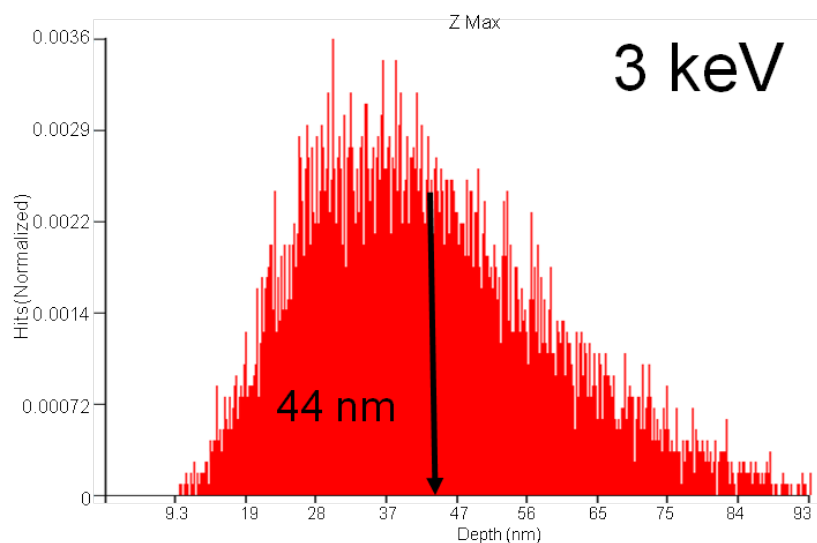


Figure D.5: CASINO simulation that shows distribution of electron penetration depths into 041 TU using a 3 keV beam energy. The simulation was run using 20,000 electrons and a beam width of 10 nm. 44 nm is the mean penetration depth.

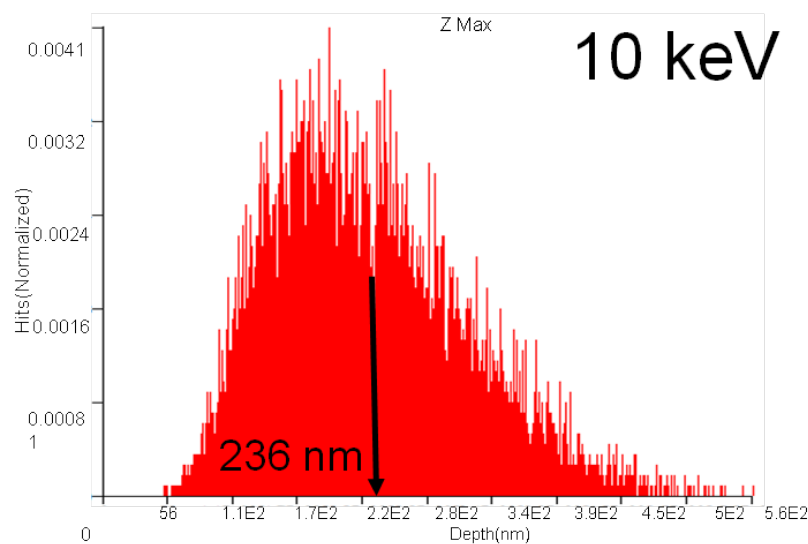


Figure D.6: CASINO simulation that shows distribution of electron penetration depths into 041 TU using a 10 keV beam energy. The simulation was run using 20,000 electrons and a beam width of 10 nm. 236 nm is the mean penetration depth.

## References

- [1] Anthonysamy, S, G Panneerselvam, Santanu Bera, SV Narasimhan, and PR Vasudeva Rao. “Studies on thermal expansion and XPS of urania–thoria solid solutions”. *Journal of nuclear materials*, 281:15–21, 2000.
- [2] Beckhoff, Burkhard, Birgit Kanngießer, Norbert Langhoff, Reiner Wedell, and Helmut H Wolff. *Handbook of practical X-Ray fluorescence analysis*. Springer, 2006.
- [3] Benz, R. “Thorium-thorium dioxide phase equilibria”. *Journal of Nuclear Materials*, 29:43–49, 1969.
- [4] Breyse, M and L Faure. “Luminescence of  $\text{Eu}^{+3}$ -activated thorium oxide”. *Journal of Luminescence*, 26(1):107–116, 1981.
- [5] Bridgman, Charles J. *Introduction to the physics of nuclear weapons effects*. Defense Threat Reduction Agency, 2001.
- [6] Castilow, Jacob. *Crystal Growth and Characterization of  $\text{ThO}_2$ ,  $\text{U}_x\text{Th}_{1-x}\text{O}_2$ , and  $\text{UO}_x$* . Master’s thesis, Air Force Institute of Technology, 2013.
- [7] Chen, Chun-Yen, Chiu-Ting Cheng, Chih-Wei Lai, Pei-Wen Wu, Kun-Chan Wu, Pi-Tai Chou, Yi-Hsuan Chou, and Hsin-Tien Chiu. “Potassium ion recognition by 15-crown-5 functionalized  $\text{CdSe/ZnS}$  quantum dots in  $\text{H}_2\text{O}$ ”. *Chemical Communications*, (3):263–265, 2006.
- [8] Colmenares, CA. “The oxidation of thorium, uranium, and plutonium”. *Progress in solid state chemistry*, 9:139–239, 1975.
- [9] Crane, TW and MP Baker. “Neutron Detectors”. *Passive Nondestructive Assay of Nuclear Materials*, 379–406, 1991.
- [10] Dunitz, JD, M Dobler, P Seiler, and RP Phizackerley. “Crystal structure analyses of 1, 4, 7, 10, 13, 16-hexaoxacyclooctadecane and its complexes with alkali thiocyanates”. *Acta Crystallographica Section B: Structural Crystallography and Crystal Chemistry*, 30:2733–2738, 1974.
- [11] Ellis, WP, AM Boring, JW Allen, LE Cox, RD Cowan, BB Pate, AJ Arko, and I Lindau. “Valence-Band photoemission intensities in thorium dioxide”. *Solid state communications*, 72(7):725–729, 1989.
- [12] Evans, William R. and David D. Allred. “Determining indices of refraction for  $\text{ThO}_2$  thin films sputtered under different bias voltages from 1.2 to 6.5 eV by spectroscopic ellipsometry”. *Thin Solid Films*, 515:847–853, September 2006.

- [13] Gruen, Dieter M. “Absorption Spectra and Electrical Conductivities of  $\text{UO}_2\text{-ThO}_2$  Solid Solutions”. *Journal of American Chemical Society*, 76(8):2117–2120, 1954.
- [14] Gubanov, V.A. “Electronic Structure and bonding in  $\text{ThO}_2$  and  $\text{UO}_2$ ”. *Solid State Communications*, 22:219–223, October 1976.
- [15] Hubert, S and P Thouvenot. “Luminescence properties of  $\text{Eu}^{3+}$  ( $4f^6$ ) and  $\text{Am}^{3+}$  ( $5f^6$ ) in thorium oxide”. *Journal of alloys and compounds*, 180(1):193–200, 1992.
- [16] Jain, RK, HS Virk, J Rama Rao, and SK Bose. “Measurement of fast neutron induced fission cross section of thorium using Lexan plastic track detector”. *Pramana*, 49(5):515–519, 1997.
- [17] Joy, David C. “An introduction to Monte Carlo simulations”. *Scanning microscopy*, 5:329–337, 1991.
- [18] Kelly, Paul J and MSS Brooks. “Electronic structure and ground-state properties of the actinide dioxides”. *Journal of the Chemical Society, Faraday Transactions 2: Molecular and Chemical Physics*, 83:1189–1203, 1987.
- [19] Kelly, T D, J C Petrosky, D Turner, J W McClory, JM Mann, JW Kolis, Xin Zhang, and P A Dowben. “The unoccupied electronic structure characterization of hydrothermally grown  $\text{ThO}_2$  single crystals”. *Physica Status Solidi ((RRL)-Rapid Reseach Letters*, doi:10.1002/pssr.201308286, 7 Jan 2014.
- [20] Kimball Physics Inc., 311 Kimball Hill Road. *EFG-7/EGPS-1017 Electron Gun and Power Supply System Technical Manual*, 2005.
- [21] Klein, Claude A. “Bandgap dependence and related features of radiation ionization energies in semiconductors”. *Journal of Applied Physics*, 39:2029–2038, 1968.
- [22] Lee, Michael. *Cathodoluminescent Study of  $\text{ThO}_2$* . Master’s thesis, Air Force Institute of Technology, 2013.
- [23] Lim, Hunhwa, Y Yun, K Park, and Kun Woo Song. “Electronic structure of uranium dioxide”. *J. Nuc. Sci. Tech*, 3:110–113, 2002.
- [24] Linares, Robert C. “Growth and properties of  $\text{CeO}_2$  and  $\text{ThO}_2$  single crystals”. *Journal of Physics and Chemistry of Solids*, 28:1285–1291, 1967.
- [25] Mann, Matthew, Daniel Thompson, Karn Serivalsatit, Terry M Tritt, John Ballato, and Joseph Kolis. “Hydrothermal Growth and Thermal Property Characterization of  $\text{ThO}_2$  Single Crystals”. *Crystal Growth & Design*, 10:2146–2151, 2010.
- [26] Martin, Paul, David J Cooke, and Robert Cywinski. “A molecular dynamics study of the thermal properties of thorium oxide”. *Journal of Applied Physics*, 112:073507–073507, 2012.

- [27] Matyssek, Christian, Vladimir Schmidt, Wolfram Hergert, and Thomas Wriedt. “The T-Matrix method in electron energy loss and cathodoluminescence spectroscopy calculations for metallic nano-particles”. *Ultramicroscopy*, 117:46–52, 2012.
- [28] Neeley, VI, JB Gruber, and WJ Gray. “F Centers in thorium oxide”. *Physical Review*, 158(3):809, 1967.
- [29] O’Hanlon, John F. *A user’s guide to vacuum technology*. John Wiley and Sons, 2005.
- [30] Olsher, U, Hadar Feinberg, Felix Frolov, G Shoham, et al. “The picrate anion as a versatile chelating counter-ion for the complexation of alkali and alkaline earth metal cations with ionophores: The ‘picrate effect’”. *Pure and applied chemistry*, 68:1195–1199, 1996.
- [31] Ozawa, Lyuji. *Cathodoluminescence: theory and applications*. Kodansha, 1990.
- [32] Pierce, BJ and RL Hengehold. “Depth-resolved cathodoluminescence of ion-implanted layers in zinc oxide”. *Journal of Applied Physics*, 47:644–651, 1976.
- [33] Pillai, CGS and P Raj. “Thermal conductivity of ThO<sub>2</sub> and Th<sub>0.98</sub>UO<sub>0.02</sub>O<sub>2</sub>”. *Journal of nuclear materials*, 277(1):116–119, 2000.
- [34] Press, William H, Brian P Flannery, Saul A Teukolsky, and William T Vetterling. *Numerical recipes: the art of scientific computings*. 1987.
- [35] Seaborg, Glenn Theodore. *Modern Alchemy: Selected Papers of Glenn T. Seaborg*, volume 20. World Scientific, 1994.
- [36] Skomurski, FN, LC Shuller, U Becker, and RC Ewing. “The corrosion of UO<sub>2</sub> versus ThO<sub>2</sub>: A quantum mechanical investigation”. *Geochimica et Cosmochimica Acta Supplement*, 69:411, 2005.
- [37] Sokolov, F, K Fukuda, and HP Nawada. “Thorium fuel cycle-Potential benefits and challenges”. *IAEA TECDOC*, Vienna, 1450, ISBN 92-0-103405-9, 2005.
- [38] Szpunar, Barbara and Jerzy Szpunar. “Thoria enhancement of nuclear reactor safety”. *Physics International*, 4(2):110, 2013.
- [39] Teterin, Anton Yu et al. “Valence electronic state density in thorium dioxide”. *Nuclear Technology and Radiation Protection*, 23:34–42, Oct 2008.
- [40] Teterin, Yu A, V.A. Terekhov, A. Yu Teterin, K.E. Ivanov, I.O. Utkin, A.M. Lebedev, and L. Vukchevich. “Inner valence molecular orbitals and structure of the X-ray O<sub>4,5</sub>(Th,U) emission spectra in thorium and uranium oxides”. *Journal of Electron Spectroscopy and related phenomena*, 96:229–236, 1998.
- [41] Veal, BW and DJ Lam. “X-ray photoelectron studies of thorium, uranium and their dioxides”. *Physical Review B*, 10(12):4902, 1974.

- [42] Vook, RW, CA Colmenares, RL Smith, and RG Gutmacher. “Cathodoluminescence of thorium in the presence of O<sub>2</sub>, CO and gas mixtures of CO-O<sub>2</sub> and CO-H<sub>2</sub>”. *Journal of Luminescence*, 27:115–126, 1982.
- [43] Winer, K, C Colmenares, and F Wooten. “Cathodoluminescence of uranium oxides”. *Journal of Luminescence*, 31:357–359, 1984.
- [44] Winter, Mark J. “WebElements periodic table”, 1993. URL <https://www.webelements.com>.
- [45] Yacobi, Ben G and David Basil Holt. *Cathodoluminescence microscopy of inorganic solids*. Springer, 1990.
- [46] Yun, Younsuk, Hanchul Kim, Hunhwa Lim, and Kwangheon Park. “Electronic structure of UO<sub>2</sub> from the density functional theory with on-site coulomb repulsion”. *Journal of the Korean Physical Society*, 50(5):1285–1289, 2007.

<b>REPORT DOCUMENTATION PAGE</b>					<i>Form Approved</i> <b>OMB No. 0704-0188</b>	
The public reporting burden for this collection of information is estimated to average 1 hour per response, including the time for reviewing instructions, searching existing data sources, gathering and maintaining the data needed, and completing and reviewing the collection of information. Send comments regarding this burden estimate or any other aspect of this collection of information, including suggestions for reducing this burden to Department of Defense, Washington Headquarters Services, Directorate for Information Operations and Reports (0704-0188), 1215 Jefferson Davis Highway, Suite 1204, Arlington, VA 22202-4302. Respondents should be aware that notwithstanding any other provision of law, no person shall be subject to any penalty for failing to comply with a collection of information if it does not display a currently valid OMB control number. <b>PLEASE DO NOT RETURN YOUR FORM TO THE ABOVE ADDRESS.</b>						
<b>1. REPORT DATE (DD-MM-YYYY)</b> 27-03-2014		<b>2. REPORT TYPE</b> Master's Thesis		<b>3. DATES COVERED (From — To)</b> Oct 2013–Mar 2014		
<b>4. TITLE AND SUBTITLE</b>  Band Gap Transition Studies of U:ThO <sub>2</sub> Using Cathodoluminescence				<b>5a. CONTRACT NUMBER</b>  <b>5b. GRANT NUMBER</b>  <b>5c. PROGRAM ELEMENT NUMBER</b>		
<b>6. AUTHOR(S)</b>  Reding, Joshua D., Second Lieutenant, USAF				<b>5d. PROJECT NUMBER</b>  <b>5e. TASK NUMBER</b>  <b>5f. WORK UNIT NUMBER</b>		
<b>7. PERFORMING ORGANIZATION NAME(S) AND ADDRESS(ES)</b> Air Force Institute of Technology Graduate School of Engineering and Management (AFIT/EN) 2950 Hobson Way WPAFB, OH 45433-7765				<b>8. PERFORMING ORGANIZATION REPORT NUMBER</b>  AFIT-ENP-14-M-31		
<b>9. SPONSORING / MONITORING AGENCY NAME(S) AND ADDRESS(ES)</b> William Ulicny Domestic Nuclear Detection Office 245 Murray Lane SW, Mailstop 0550 Washington DC 20528-0550 william.ulicny@dhs.gov				<b>10. SPONSOR/MONITOR'S ACRONYM(S)</b>  DNDO		
<b>12. DISTRIBUTION / AVAILABILITY STATEMENT</b> DISTRIBUTION STATEMENT A: APPROVED FOR PUBLIC RELEASE; DISTRIBUTION UNLIMITED				<b>11. SPONSOR/MONITOR'S REPORT NUMBER(S)</b>		
<b>13. SUPPLEMENTARY NOTES</b> This material is declared a work of the U.S. Government and not subject to copyright protection in the United States.						
<b>14. ABSTRACT</b> The Department of Defense has expressed interest in thorium dioxide (ThO <sub>2</sub> ) and uranium dioxide (UO <sub>2</sub> ) as possible candidates for use as special nuclear material in designing neutron detectors. Both materials have large neutron interaction cross sections. Uranium dioxide is particularly attractive due to its semiconducting properties and a relatively small band gap of 2 eV. Both materials fluoresce under ionizing radiation making them candidates for scintillating detectors. Three U <sub>x</sub> :Th <sub>1-x</sub> O <sub>2</sub> (x= 0.00, 0.01, 0.22) hydrothermally grown single crystals were examined using cathodoluminescence to interrogate the changing electronic properties of ThO <sub>2</sub> as it became an alloy. Both depth-resolved and temperature-dependent cathodoluminescence studies were performed to examine the crystal structure and the defects present. An ultra-high vacuum system operating at 10 <sup>-8</sup> Torr was used with electron beam energies ranging from 2 to 14 keV. Spectra were taken on all three samples before and after a proprietary chemical cleaning process involving a crown ether/picric acid solution was applied to the crystals to remove surface contaminants. Spectral deconvolution of the spectra showed evidence of both direct and indirect gap photon transitions from the O 2p to Th 6d at 4.2 eV and 4.8 eV respectively. Uranium-doped spectra showed evidence of the midgap O 2p to U 5f quadrupole transition and O 2p to U 6d transition at 5 eV.						
<b>15. SUBJECT TERMS</b> Uranium Thorium Dioxide, Cathodoluminescence, Uranium Oxide						
<b>16. SECURITY CLASSIFICATION OF:</b>			<b>17. LIMITATION OF ABSTRACT</b>		<b>18. NUMBER OF PAGES</b>	
<b>a. REPORT</b>  U	<b>b. ABSTRACT</b>  U	<b>c. THIS PAGE</b>  U	  UU		  106	
					<b>19a. NAME OF RESPONSIBLE PERSON</b> Dr. Robert Hengehold (ENP)	
					<b>19b. TELEPHONE NUMBER (include area code)</b> (937) 255-3636 x4502 Robert.Hengehold@afit.edu	